THESIS FOR THE DEGREE OF DOCTOR OF PHILOSOPHY

RESONANT INTERACTIONS BETWEEN NANOPARTICLE PLASMONS AND MOLECULAR EXCITONS

.

GÜLIS ZENGIN

Department of Applied Physics

CHALMERS UNIVERSITY OF TECHNOLOGY

Göteborg, Sweden 2014

Resonant Interactions Between Nanoparticle Plasmons and Molecular Excitons
GÜLIS ZENGIN

Cover: Schematic diagram of a silver nanoparticle coupled to a molecular J-aggregate.

Resonant Interactions Between
Nanoparticle Plasmons and Molecular Excitons

Gülis Zengin
Department of Applied Physics
Chalmers University of Technology

Abstract

Molecular plasmonics involves the study and applications of plasmonic metal nanostructures interacting with molecules. It has been a basis for development of fundamental understandings of light-matter interactions as well as of new technologies, including biological and chemical sensors and plasmon-enhanced spectroscopies. Plasmonic nanoparticles can focus light to subwavelength volumes resulting in strong induced electromagnetic fields. When a molecule is placed in such a "hot spot", its properties can change dramatically due to modifications of the photon density of states. This thesis focuses on studies of coupled molecule-plasmon systems in which the plasmon energy coincides with a molecular exciton absorption band.

Colloidal silver nanorods and silver nanotriangles were coupled to molecular J-aggregates and studied at the single particle level. J-aggregates are attractive for studies of resonant plasmon-molecule interactions because of their narrow linewidths and high oscillator strengths. Depending on the damping rates, quality factors and mode volumes of the nanoparticle plasmon resonance, it was shown that it is possible to reach different interaction regimes, ranging from weak to strong coupling, characterized by distinct spectral profiles.

Rhodamine 6G (R6G) is a dye molecule which interactions with plasmons has been studied extensively in the context of surface-enhanced Raman spectroscopy. Thiolated R6G and ordinary R6G was adsorbed on silver nanoparticles and the scattering and absorption properties of the composite systems were compared. The thiol linker resulted in immobilization of more molecules per silver nanoparticle, which resulted in a pronounced spectral dip in the plasmon scattering spectrum qualitatively similar to the J-aggregate case. However, simulations showed that surface-enhanced absorption was the main mechanism behind the spectral changes in this case.

In addition to confining light in small volumes, plasmonic nanoparticles can also direct light under special circumstances. The last part of the thesis deals with directional scattering from bimetallic plasmonic nanoparticle antennas. It is shown that light can be scattered in different directions determined by its wavelength, that is, the plasmonic antenna constitute a nanoscale "color router".

Keywords: Localized surface plasmon resonance, nanoparticles, J-aggregates, strong coupling, Rhodamine 6G, surface-enhanced absorption

Appended Papers

The following papers are included in the thesis:

Paper 1: ***Approaching the strong coupling limit in single plasmonic nanorods interacting with J-aggregates***
Gülis Zengin, Göran Johansson, Peter Johansson, Mikael Käll, and Timur Shegai
Scientific Reports, 3, 3074 (2013).
My contribution: I participated in planning, conducting the experiments, analyzing the data, and writing the paper.

Paper 2: ***Strong plasmon-exciton coupling of single silver nanoprism with a J-aggregate***
Gülis Zengin, Martin Wersäll, Sara Nilsson, Tomasz J. Antosiewicz, André Dankert, Mikael Käll and Timur Shegai
Submitted manuscript.
My contribution: Together with Martin Wersäll, I prepared samples, conducted the optical experiments and SEM, TEM, AFM measurements, analyzed the data and wrote a draft of the paper together.

Paper 3: ***Interaction between Localized Surface Plasmons and Thiolated Rhodamine 6G***
Gülis Zengin, Tina Gschneidtner, Tomasz J. Antosiewicz, Kasper Moth-Poulsen, Mikael Käll and Timur Shegai
In manuscript.
My contribution: I conducted the optical, surface chemistry and SEM measurements. I analyzed the data. I prepared most of the samples. I wrote a draft of the paper.

Paper 4: ***A bimetallic nanoantenna for directional colour routing***
Timur Shegai, Si Chen, Vladimir D. Miljkovic, Gülis Zengin, Peter Johansson, and Mikael Käll
Nature Communications, 2, 481 (2011).
My contribution: I participated in building part of the optical setup, conducting experiments and writing the paper.

Contents

Chapter 1

Introduction

Light brings life to our world and we see the world through light. Interaction of light with matter makes it possible for us to perceive the matter. Light hits photoreceptor cells of our retina, which is the base of our sense of vision. When light interacts with matter, it can be absorbed, emitted, scattered, and/or reflected. For instance, plants doing photosynthesis absorb light and convert it into chemical energy. We perceive colors and shapes of objects depending on the properties of the object and on how light interacts with this object. For example, when we look at an object, we see its color because it reflects that color. Thus interaction of light with matter can reveal information about it. Light is an investigative tool to understand matter and therefore the world around us. This is a step forward to design and engineer new systems, which can lead to technological innovations and developments.

Controlling and manipulating light-matter interactions are the basis of many existing technologies, as well as new scientific and technological developments [1]. Advancements in nanoscale synthesis, fabrication, characterization, and computational tools made it possible to study the near-field properties of light-matter interactions at the nanoscale [2], while, formerly, research was more focused on the far-field aspect of these interactions[3,4]. Interaction of light with nanosized metal particles has led to the emerging area of plasmonics. The plasmon resonance is a coherent oscillation of the surface conduction electrons in the metal excited by electromagnetic radiation. Plasmonic metal nanostructures provide the ability to control and manipulate light at the nanometre scale [5–8].

One of the most important properties of plasmonic nanostructures is the ability to focus light to subwavelength volumes. In that sense, plasmonic nanostructures can be considered as optical resonators or cavities, an analogy that is used in some parts of this thesis. Chapter 2 describes the properties of plasmonic nanostructures from the cavity perspective and defines related properties of optical cavities. When plasmonic nanostructures are compared with traditional cavities, such as micropillars and photonic crystals, they have both advantages and disadvantages. The main advantage of the plasmonic nanostructures is that they can squeeze light into volumes much smaller than the diffraction limit and the effective mode volumes of other cavities. On the other hand, the quality factor of plasmonic resonances, which determines the ability of a cavity to temporally confine light, is lower than that of the other cavities due to losses. High quality factor cavities are generally preferred because they allow for longer interaction times and stronger coupling to

molecules interacting with the cavity. However, having a high quality factor also restricts the bandwidth and increases the time it takes to reemit photon that has been absorbed in the cavity. Another disadvantage of having a high quality factor is the size of the cavity, because high quality factor cavities are usually larger. This results in a large size mismatch between the cavity and the emitter, which becomes a challenge when designing and realizing subwavelength and strongly interacting plasmon-emitter systems. Therefore, even though plasmonic nanostructures have relatively low quality factors, their subwavelength effective mode volumes may overcome these disadvantages and maybe eventually become better alternatives. For instance, single-photon sources on a chip at optical frequencies with high operation speed based on plasmonic nanostructures have been proposed [9].

Another important advantage of plasmonic nanostructures is that they can act as nanoantennas that can manipulate and direct light [10–12]. This property of plasmonic nanostructures is described in Chapter 2. When light is focused in a small volume by a antenna, one might think that light inherently leaves the antenna in a directed way. However it is not that straightforward. Antennas are needed to collect and couple light into free space propagation in an efficient way. Plasmonic nanostructures can be designed to give light directional emission by means of different symmetry breaking mechanisms with resulting effect of interference. This occurs via plasmon-plasmon interaction. In Paper 4, directional emission from plasmonic nanoparticles is demonstrated by using bimetallic particle dimers. In Chapter 2, an unpublished continuation study of Paper 4 is also presented.

Understanding properties of plasmonic nanostructures by using the cavity analogy helps us study the interaction of plasmonic nanostructures with molecules or emitters, a field usually referred to as molecular plasmonics. Since the interaction between surface plasmons and nearby molecules constitutes the basics of many applications and technologies, the study of molecule-plasmon interactions, became a significant sub-field of plasmonics. Even though molecule-plasmon interactions has been a subject of former studies, there are many gaps in the current understanding of the field. One reason is that a precise spatial and spectral control of plasmonic nanostructures as well as positioning of molecules near metal surfaces are needed for effective molecule-plasmon interactions. This requires advanced nanofabrication, chemical synthesis, surface and molecular functionalization, molecular self-assembly, and accurate measurements and computational tools to model, design, control, and characterize molecules on metal surfaces. Therefore breakthroughs in all these areas have led to recent progress in the field of molecular plasmonics. To be more specific, developments in chemical synthesis have made it possible to synthesize highly crystalline nanoparticles of different shapes, sizes and compositions by forming particles on an atom-by-atom basis [13]. Improvements in lithography techniques have enabled fabrication of nanoparticles that are controlled in size, shape, and position on a substrate. This method is crucial to tailor the spacing of plasmonic particles, which enables controlling the particle-particle interactions. Moreover, novel methods were developed by combining chemical and lithographic techniques, such as colloidal lithography, which renders possible the

fabrication of plasmonic nanostructures over large areas [14]. Even though it is still a challenge to precisely, specifically and selectively position molecules in a certain configuration and orientation on metal nanostructures in a robust way, different surface functionalization techniques have been developed by using chemical bonds, electrostatic interactions or biological recognitions. Molecular self-assembly has become a powerful way to immobilize molecules on metal surfaces [13]. Advances in optical imaging and spectroscopy techniques, such as single particle dark-field microscopy and hyper spectral imaging, facilitate the measurement of plasmon-molecule nanocomplexes on a single particle level. This provides detailed information about the properties of nanostructures that are not measurable on the ensemble level [7]. These improvements in both plasmonics and molecular nanotechnology have progressively shifted the focus of molecular plasmonics from developing plasmonic molecule complexes and investigating their physical properties to the potential applications of these complexes. The broad spectrum of applications includes biological and chemical sensors [15], surface-enhanced spectroscopies [16,17] , plasmon resonance energy transfer (PRET) [18,19], plasmon enhanced solar light harvesting [20], near-field scanning optical microscopy [21], single molecule detectors [22], targeted delivery [23], optical tweezers [24] and optical switches of gene interference [25]. In fluorescence-based applications, interactions of metal nanostructures with fluorophores can have many useful effects, including increased quantum yields, increased photostability, increased distances for resonance energy transfer, and decreased lifetimes. These changes can result in improved sensitivity and photostability and decreased interference from unwanted background emission [26].

Molecules can interact with plasmonic nanostructures optically, thermally or mechanically [13]. In this thesis, I focus on the optical mode of interaction. Localized surface plasmon resonance (LSPR) based sensing [27], surface enhanced fluorescence (SEF) [28], surface-enhanced Raman spectroscopy (SERS) [29], molecule-plasmon hybridization [30], and plasmon energy transfer (PRET) [18] are examples of optical interaction. Optical interaction between molecules and collective excitation of conduction electrons in metal nanoparticles substantially depends on the electronic structure of molecules. If the molecule has resonant absorbance overlapping with that of the surface plasmons, we can observe plasmon resonant energy transfer or plasmon hybridization.

In Chapter 3 the basic properties of molecular optical excitation are discussed with a focus on Rhodamine 6G and molecular J-aggregate, which are the subjects of Paper 1, Paper 2 and Paper 3. Chapter 4 provides a background to some of the plasmon-molecule interactions starting with refractive index dependent plasmonic resonance sensing. This method was used to measure the kinetics of streptavidin coated quantum dot binding on gold nanoparticles for directional emission of bimetallic nanoantennas. The principles of surface enhanced Raman spectroscopy (SERS) and surface enhanced fluorescence (SEF) are then described. SEF is related to Purcell effect, which also makes a connection with cavity properties of plasmonic nanoparticles. I then briefly discuss Förster Resonance Energy Transfer (FRET) and

my unpublished preliminary results on plasmon enhanced FRET of fluorescent proteins in mammalian cell membranes. Finally, resonance coupling is presented from two different perspectives, the coupled harmonic oscillator model and the cavity perspective, with analogies in cavity quantum electrodynamics. Paper 1 and Paper 2 focus on the importance of reaching the so-called strong coupling regime. A strongly coupled light-emitter system is important because it can enable photon-photon interactions at the single-photon level due to its nonlinear energy structure. This is because photon-photon interactions are quite weak and require nonlinearity [9]. This effect is known as photon blockade in cavity quantum electrodynamics (CQED) analogy [31]. There has been a report about this effect with plasmonic nanostructures [32]. Single photon transistors are another possible application of strongly coupled plasmon-emitter systems [33,34]. The strong coupling regime in plasmonics has also been proposed as a means to enhancing chemical reactions [35].

In Chapter 4, surface chemistry, fabrication, and optical measurement techniques are described. The thesis ends with Chapter 5, presenting outlook and a summary of the appended papers.

Chapter 2

Surface Plasmons in Nanoparticles

This chapter focuses on the basic properties of the surface plasmons, such as the ability to focus light in subdiffraction volumes and to manipulate and direct light at the nanoscale. This chapter also describes how plasmonic nanoparticles supporting surface plasmons can be considered as cavities, which will help to understand plasmon-exciton interactions later in Chapter 4. The properties of silver nanotriangles as a cavity are compared with other cavities. Silver nanoparticles are chosen in this comparison because they were studied in Paper 1 and Paper 2 in terms of plasmon-exciton interaction resulting in different interaction regimes, from weak to strong coupling.

In addition to the ability to focus light into small volumes, plasmonic nanoparticles can also manipulate and direct light at the nanoscale functioning as nanoantennas. Plasmon-plasmon interaction is the basis of the directional light emission. Directionality can be achieved in different ways but the fundamentals lie in coupling of different plasmonic components resulting in interference and, as a consequence, directional emission into the far field [36]. In this chapter basic concepts of directionality are given as the background for Paper 4, after which the unpublished continuation work of Paper 4 is presented.

Plasmon oscillations can be described by classical physics, in which the collective oscillations of free electrons in metals are modeled as a damped harmonic oscillator, in other words the Lorentz model. An external electric field gives rise to a displacement of the electron gas with respect to the ionic cores [37]. This induces a restoring electric field inside and outside the particle. If there is a non-absorbing molecule or a solvent with high dielectric function in the close vicinity of the plasmonic particle, these restoring forces become weaker by shifting the plasmon resonance to lower energies (redshift in wavelength) [38]. The relation between the polarizability of a subwavelength spherical nanoparticle and the dielectric function of the surrounding medium (alternatively, refractive index) can be understood from the following formula based on the quasi-static approximation. The complex polarizability defining the dipole moment inside the metal particle induced by the external field is given as [39]:

$$\alpha(\omega) = 4\pi a^3 \frac{\varepsilon_{metal}(\omega) - \varepsilon_{medium}}{\varepsilon_{metal}(\omega) + 2\varepsilon_{medium}} \qquad (2.1)$$

Here, a is the radius of the spherical particle. The dielectric function of the metal can be approximated by the free electron Drude model with ω_p as the plasma frequency and γ as the damping factor:

$$\varepsilon_{metal}(\omega) = 1 - \frac{\omega_p^2}{\omega^2 + i\omega\gamma} \tag{2.2}$$

The polarizability undergoes a resonance when the real part of the dominator vanishes ($Re[\varepsilon_{metal}(\omega) = -2\varepsilon_{medium}]$) and $Im[\varepsilon_{metal}(\omega)]$ is small or slowly varying. By using the complex polarizability, the scattering, absorption and extinction cross sections can be calculated via the Poynting vector, where $\varepsilon_{metal} = \varepsilon_1 + i\varepsilon_2$ [40].

$$C_{sca} = \frac{k^4}{6\pi}|\alpha|^2 = \frac{8\pi}{3}k^4 a^6 \left|\frac{\varepsilon_{metal}(\omega) - \varepsilon_{medium}}{\varepsilon_{metal}(\omega) + 2\varepsilon_{medium}}\right|^2 \tag{2.3}$$

$$C_{abs} = kIm[\alpha] = 4\pi k a^3 Im\left[\frac{\varepsilon_{metal}(\omega) - \varepsilon_{medium}}{\varepsilon_{metal}(\omega) + 2\varepsilon_{medium}}\right] \tag{2.4}$$

$$C_{ext} = C_{sca} + C_{abs} \tag{2.5}$$

2.1 Optical resonators

Optical resonators confine and store light at resonance frequencies which are determined by their geometrical dimensions and constituent materials. Within a resonator, light circulates or is repeatedly reflected. Fabry-Perot resonators, microdisks, and photonics crystals are some of the typical examples of optical cavities. Optical resonators are characterized by two parameters: the mode volume and the quality factor [41].

The mode volume V_{eff} (or effective volume) describes the degree of spatial light confinement. It is defined as the volume of the confined optical mode and expressed with the following formula:

$$V_{eff} = \frac{\int \varepsilon(\boldsymbol{r})|\boldsymbol{E}(\boldsymbol{r})|^2 d^3\boldsymbol{r}}{max(\varepsilon(\boldsymbol{r})|\boldsymbol{E}(\boldsymbol{r})|^2)} \tag{2.6}$$

$\varepsilon(\boldsymbol{r})$ is the dielectric constant and $|E(\boldsymbol{r})|$ is the strength of electric field in the cavity [42,43]. The denominator is the maximum value of the product of the dielectric constant and the strength of the electric field over all $\boldsymbol{r}$.

The second parameter is the quality factor (Q), which represents the degree of temporal light confinement in the cavity. It is a dimensionless parameter that describes the time in which ,light can be stored, relative to the optical period of the mode of confined light. A large quality factor indicates low-loss in the cavity. It is defined by the ratio of the stored energy in the cavity to the energy loss per optical cycle of the confined light [41]:

$$Q = 2\pi \frac{energy\ stored}{energy\ loss\ per\ cycle} \tag{2.7}$$

As the stored energy E is lost at the rate $c\alpha_r E/v_0$ (per cycle of the optical field) and as α_r is the loss coefficient of the cavity, then the quality factor can be written as following:

$$Q = \frac{2\pi v_0}{c\alpha_r} \tag{2.8}$$

By substituting the spectral width which is given by $\Gamma = c\alpha_r/2\pi$, the quality factor becomes equal to

$$Q = \frac{\omega_0}{\Gamma} \tag{2.9}$$

2.2 Plasmonic nanoparticles as cavities

Optical resonators, or cavities, consist of a closed structure that can confine electromagnetic fields within a small volume and yield large field enhancement [43,44]. Similarly, metallic nanostructures can also concentrate light and produce high local field intensities [45]. Light incident on plasmonic nanoparticles applies a force on the gas of electrons inside the nanoparticle and drives them into the collective oscillations, which is known as a surface plasmon. At a certain light frequency, a collective oscillation of the electrons are resonantly driven, resulting in a strongly confined field which is known as hot spots [5,46]. Charges concentrate at the apex of plasmonic nanoparticles. Therefore, plasmonic nanoparticles having sharp edges such as rods, triangles and cones, can give higher field enhancement compared to spherical particles [46]. High field enhancement can be also be achieved by having a small gap between plasmonic nanoparticles, where the charges of opposite signs build up across the gap [5,46–49][46,50–52]. Figure 2.1 shows examples of charge distributions and hot spots in commonly used plasmonic nanostructures. The blue arrows represent the polarization of the incident field. The charge distribution and the modes shown in Figure 2.1 are only some examples of the possible oscillations, and the plasmonic nanostructures here presented can support different, including higher order modes. For instance, for the nanorod the longitudinal mode is given and the transverse mode can be excited by perpendicular polarization. For the nanotriangles, one of the possible dipole modes is illustrated.
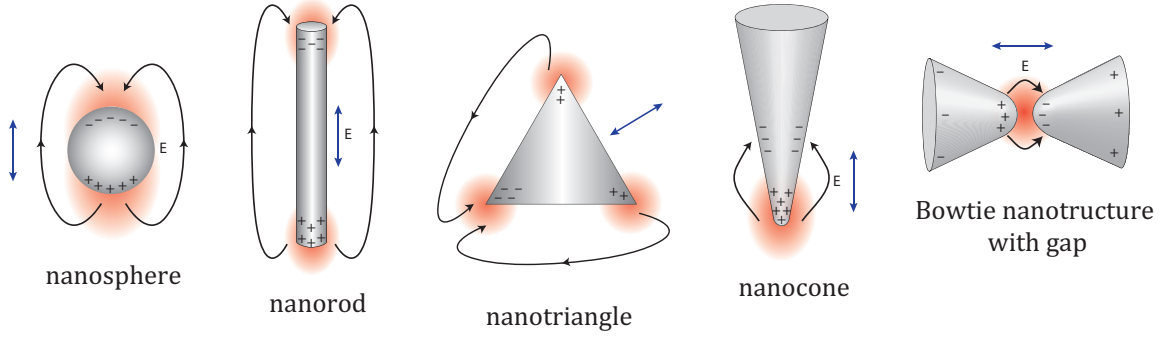
Figure 2.1 - Illustration of induced charge distribution and associated field enhancement in commonly used metallic nanostructures. Reproduced from [46,50–52].

While plasmonic nanostructures can confine light into intense and engineered localized fields at deep-subwavelength volumes, dielectric resonators are limited to focusing on about half a wavelength $\sim (\lambda/2)$ with mode volumes $\sim (\lambda/2)^3$, where λ is the wavelength of light inside the dielectric medium [5]. With this advantage over dielectric resonators, plasmonic nanoparticles can have an important effect on the efficiency of many optical processes, such as tailoring light–matter interactions at the fundamental level, which requires high quality factors and small mode volumes. Even though plasmonic nanoparticles usually have small quality factors, which are usually between 10-100, by having small mode volumes they can still perform better than dielectric cavities with high quality factors (10^6) giving a broader response and simpler electrical access [5].

Similar to the derivation for the quality factor of optical resonators (equation 2.10), the scattering, absorption, and extinction cross-sections of a plasmonic nanoparticle have a Lorentzian shape centered at ω_1 with a full width at half maximum (FWHM) $\Delta\omega_1 = \Gamma_1$:

$$\propto \frac{1}{\left(\omega - \omega_{pl}\right)^2 + \left(\Gamma_{pl}\right)^2} \tag{2.10}$$

Therefore, the quality factor of plasmonic nanocavities follow the same formulation: $Q = \omega_{pl}/\Gamma_{pl}$. The parameters affecting the resonance properties of plasmonic nanoparticles, such as shape, size, material type and crystallinity, can change the damping rate and thus the quality factor. Figure 2.2 (a, b, c) compares a gold nanorod and nanosphere in terms of linewidth and quality factor. Figure 2.2 (a) shows the scattering spectra of a gold nanorod 100 nm in length and ca. 15-25 nm in width and height and a gold nanosphere with a 60 nm diameter. The nanorod has a much smaller volume than the nanosphere. Both particles are monocrystalline. Figure 2.2 (b) shows linewidths of various nanorods and nanosphere of different sizes versus the peak position of the plasmon peak. Dephasing times, which are deduced from $2\hbar/\Gamma$, are plotted on the right side of the same plot. The linewidth of

8

nanospheres decreases (dephasing time increases) when particles become smaller, due to suppressed radiation decay. The linewidth of nanorods decreases with higher aspect ratios and reaches a limit. This is because in such small nanorods radiative decay is already small and nonradiative decay decreases with increasing an aspect ratio due to interband transitions [53].
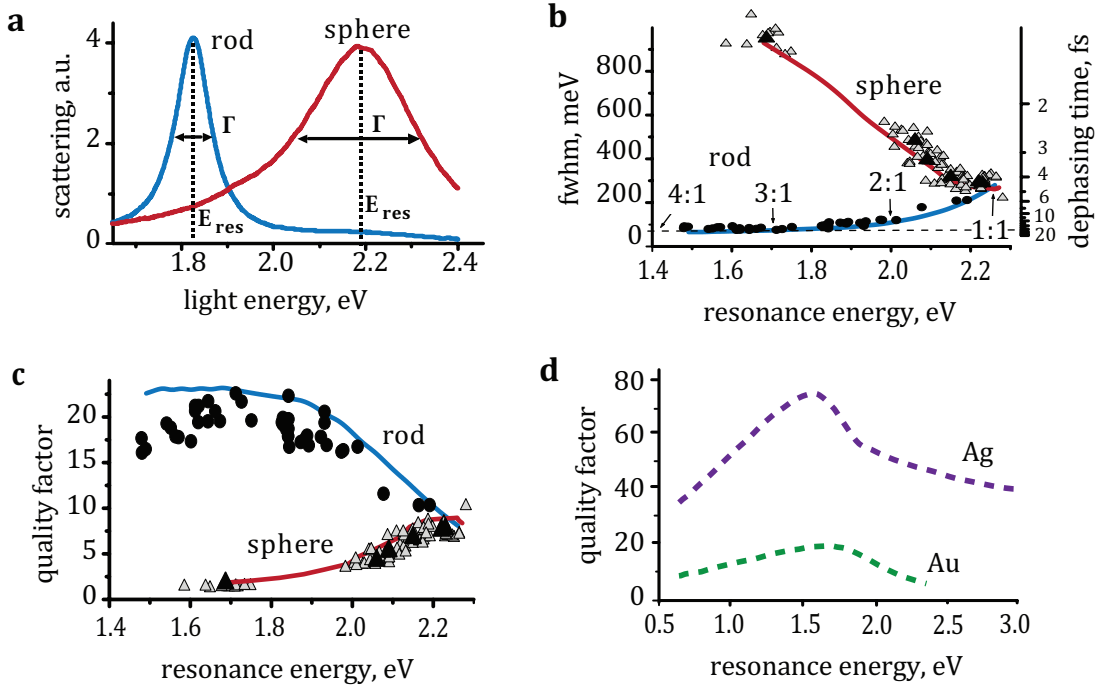
Figure 2.2 – (a) Scattering spectra of a gold nanorod and nanosphere under illumination conditions where the incident light is polarized along the long rod axis. The resonance energies and linewidths are marked. (b) Linewidth of plasmon resonances in nanorods (black dots) and nanospheres (open triangles) are plotted as resonance energy. The right part of the plot shows the corresponding dephasing times. The black triangles are the nanospheres with diameter 150, 100, 80, 60, 40, 20 nm from left to right. Different aspect ratios for nanorod are indicated in the plot. Solid lines show the calculated results. (c) Quality factor of the same particles are plotted as a function of resonance energy for both nanorods and nanospheres. (Reproduced from [53]) (d) Quality factor versus resonance energy is given for silver and gold nanoparticles (Reproduced from [50])

Quality factors (E_{res}/Γ) of the same particles are plotted in Figure 2.2 (c). In the case of plasmonic nanoparticles, the quality factor is related to the local field enhancement. The nanospheres have lower quality factor and field enhancement factors than the nanorods due to radiative damping for large particles and interband damping for small particles [54]. Interband damping is suppressed in the nanorod case; therefore they have higher quality factors and local-field enhancements [53].

9

The Q factor of the plasmonic nanoparticles also depends on material and the dielectric function of the metal at the given plasmon frequency as shown in Figure 2.2 (d). [50], [55]. Silver nanoparticles are better than gold nanoparticles in terms of quality factor and field enhancement. Note than in Figure 2.2 (d) radiation losses and surface imperfection are neglected [50].

Crystallinity is another parameter that can influence losses and quality factor of a plasmonic cavity. Losses are determined both by Ohmic losses and scattering at grain boundaries. It has been shown that polycrystalline gold film has higher losses and shorter propagation lengths compared to single-crystalline gold [56]. Grain size also affects the losses. Smaller grain sized plasmonic nanocavities have additional losses due to the grain boundary scattering compared to bigger grain sized cavities [57]. The reason for the scattering lies mainly in inhomogeneities of the free-electron gas due to grain boundaries [56].

2.3 Plasmonic cavities versus other cavities

Plasmonic nanoparticles have both advantages and disadvantages compared to other cavities. They can localize light in volumes significantly smaller than the diffraction limit of light and therefore the effective mode volume is significantly smaller than in other cavities [58]. Having a small mode volume makes it easier to fill the mode volume with emitters and thus to enter the strong coupling regime. By confining light the plasmonic cavities can significantly alter the photonic density of states and thus the dynamics of light-matter interactions, such as enhancement of spontaneous emission of an emitter in a cavity [9]. Therefore, the ratio of the spontaneous emission rate near/in the cavity to that in free space, the Purcell factor, is higher in plasmonic cavities. On the other hand, they suffer from losses and low quality factor compared to other cavities. Although surface plasmons are well known for having large losses, there are also attractive for building devices that can exploit this lossy nature for controlling dissipative quantum dynamics [9,59]. The summary of the comparison of different cavities is given in Figure 2.3 with related cavity parameters.

Cavity	Length = 42.2 μm Width = 23.4 μm	Photonic Crystal Slab	Micropillar	Microdisk	Ag Nanotriangle
λ (nm)	852.4	1182	937	744	589
E (eV)	1.45	1.32	1.32	1.66	2.11
Q	4.4×10^7	6000	7350	12000	5 - 20
V (μm^3)	18148	0.04	0.3	0.07	0.4×10^{-6} - 1.4×10^{-6}
F_p	114	441	36	125	8×10^4 - 6×10^5
$\kappa\pi/2$ (meV)	3.3×10^{-5}	0.22	0.18	0.14	106 - 422

Figure 2.3 – Comparison of properties of different cavities. Reproduced from [60].

Understanding plasmonic nanoparticles from the cavity perspective is important because it provides a perspective for studying plasmon-emitter interaction. In Chapter 4, the comparison of the same cavities will be extended to their interaction with emitters in terms of different properties. Before studying plasmon-exciton interaction, properties of plasmonic nanoparticles and plasmon-plasmon interaction will be described in the following section. This section is the basis for the Paper 4 and presents the unpublished continuation work of Paper 4.

2.4 Directional emission of quantum dot integrated bimetallic nanoantennas

After the light leaves the cavity, directional emission may be considered as an inherent property. Antennas are used to mediate directional light emission. Let us consider a Hertzian dipole, which is the simplest form of a radiating element. If we compare the radiation of a Hertzian dipole and a half-wavelength dipole antenna, the dipole antenna facilitates more efficient coupling of the current source to free space radiation modes, resulting in amplified and redirected emission as shown in Figure 2.4 [61].
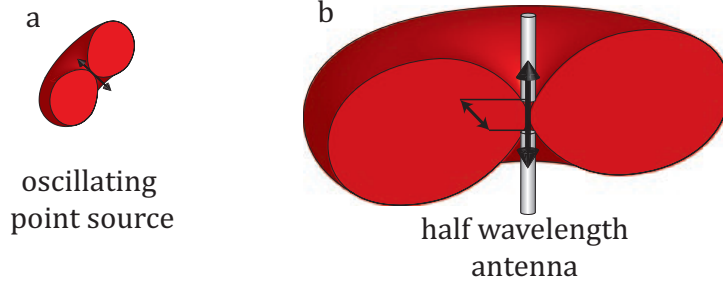
Figure 2.4 - Emission from (a) a Hertzian dipole (the arrow indicates the direction of the current and the orientation of the dipole) (b) a half wavelength antenna [61].

Plasmonic nanostructures can function as antennas at the nanoscale by collecting radiation of an emitter from certain directions and redirecting the radiation to free-space propagation of light, by reciprocity [62]. If the coupling of the emitter to a nanoantenna mode overcomes the direct coupling of the emitter to the far field, the mode of the nanoantenna determines the emission of the emitter [12,62,63]. Then the nanoantenna can be considered as a mediating element between near field and far field [64].

Directional emission from a nanoantenna is characterized by directivity. Directivity, $D(\theta, \phi)$, is a figure of merit for an antenna and it is defined as the power $P(\theta, \phi)$ per unit solid angle emitted from the antenna in a certain direction versus the power per solid angle emitted from an isotropic source, which emits uniformly in all directions, radiating the same total power [65].

$$D(\theta, \phi) = 4\pi \frac{P(\theta, \phi)}{\int P(\theta, \phi) \, d\Omega} \tag{2.11}$$

In other words, it describes how much the antenna radiates in a certain direction compared to the average value over all directions. To obtain strong directionality with plasmonic nanoantennas, spatial phase retardation between antenna elements are typically used. Yagi–Uda antennas, made of multi-element arrays, are one of the examples of such antennas. They consist of a locally driven feed element that is coupled to several director elements that collectively interfere in the far field, to produce directional emission [11], [66]. However, the design and fabrication of these types of antennas are complex and the resulting antennas are not compact [36]. Another way to obtain strong directionality is by using a single element antenna if interference between electric dipole and higher-order multipole parts can be achieved [67,68].

While single element antennas are easier in terms of design and fabrication, efficient excitation of higher-order magnetic and electric multipoles is a challenge. Strong field gradients on the scale of the nanoparticle are needed, excitation with simple plane wave illumination is hard [36]. Another method for obtaining strong

directionality by plasmonic nanoparticles is by manipulating the phase by introducing an asymmetrical material composition as proposed in Paper 4 and the continuation work presented in this chapter. Based on our results presented in Paper 4, we continued to study directionality of bimetallic nanoantennas in both vertical and horizontal configurations, aiming at attaching quantum dots and measuring the directional emission of the attached quantum dots.

The results obtained for directional vertical bimetallic nanoantennas are shown in Figure 2.5 (a). A vertical bimetallic nanoantenna configuration is used because of simpler design and fabrication and easier access for quantum dot attachment. Scanning electron microscopy images show the structure of the nanoantennas. The bottom disk is made of Ag with diameter 150 nm and height 40 nm. The top disk is made of Au having 30 nm height and ~80-100 nm diameter size depending on the spacer thickness between bottom and top disks. The two disks were separated by a 30 nm Al_2O_3 layer. The idea behind this configuration is that the bottom Ag disk performs the role of a reflector element and the top Au disk performs the role of a feed element in the antenna structure. When the nanoantenna is excited with an incoming light from the top (Au side), it gives a higher localized field around the Au disk than if the situation is reversed. The calculated near-field intensity at 730 nm (n=1.5) for the structure excited from top (Au disk) and bottom (Ag disk) as shown in Figure 2.5 (b). The contrast in intensity at the position near the Au disk is shown with red and blue arrows. The preliminary electrodynamic simulations are done by using the Green's function method. In simulations parameters for Ag disk (diameter = 145 nm, height = 40 nm) and Au disk (diameter = 85 nm, height = 30 nm) are taken. The two disks are separated by a 30 nm spacer. Figure 2.5 (c) shows the calculated front-to-back ratio (F/B) in this configuration. A point-dipole source is positioned 5 nm to one side of the Au disk. The enhancement factor was calculated by quantifying the radiation pattern of a point dipole with and without an antenna. There is a good agreement between the F/B ratio and enhancement factor. The radiation pattern for a dipole placed 5 nm away from the Au disk was calculated at 730 nm in φ=0 plane and shown in Figure 2.5 (d).

For optical measurements, three different samples were prepared by varying the Al_2O_3 layer thicknesses 30 nm, 40 nm and 50 nm in order to test the effect of the spacer thickness. Figure 2.6 shows SEM images in the first row and the corresponding optical measurements of the nanoantennas in the second row. Nanoantennas are excited by unpolarized white light illumination from a fiber-coupled halogen lamp at normal incidence onto the samples. Transmitted and reflected lights is measured by a fiber-coupled spectrometer. Absorption spectra are calculated from transmission and reflection spectra (A = 1–T-R).
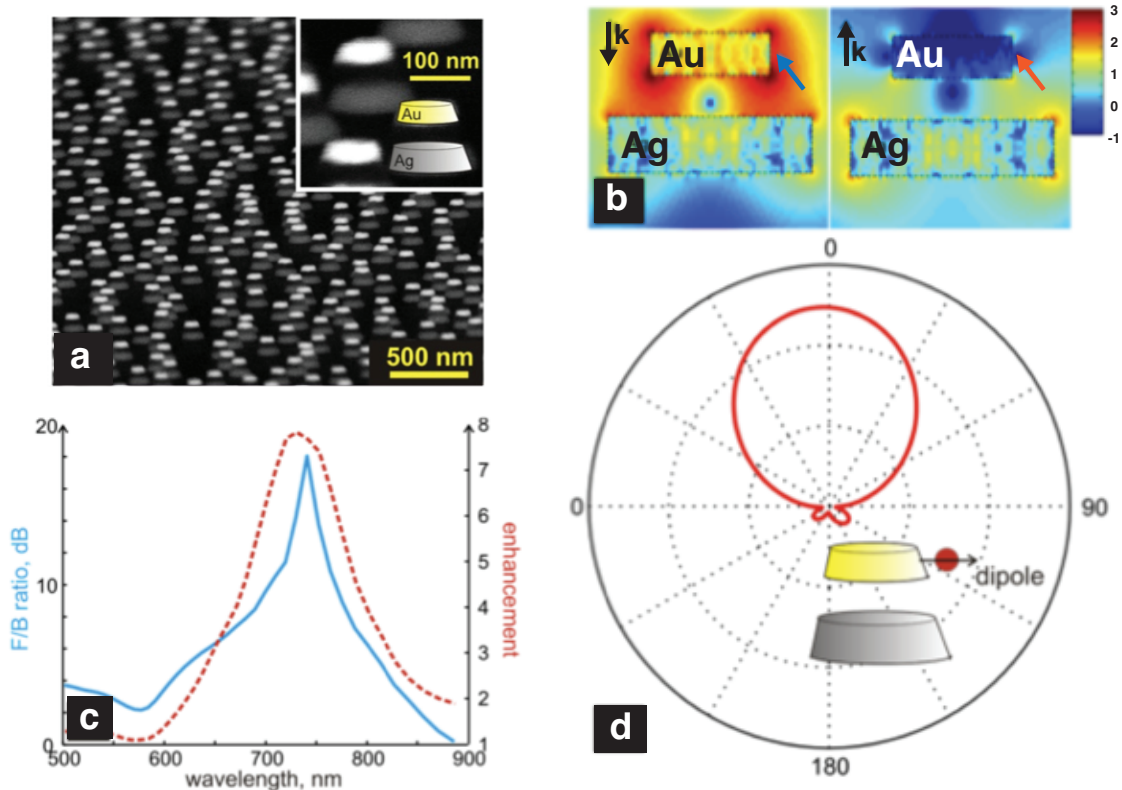
Figure 2.5 – (a) Scanning electron microcopy images of the vertical bimetallic nanoantennas. (b) Calculated near-field intensity at 730 nm for the nanoantenna excited from top (Au side) and bottom (Ag side). (c) Forward to backward ratio and enhancement for the nanoantenna for a dipole positioned 5 nm away from the upper Au disk. (d) Calculated radiation pattern for the same dipole.

Nanoantennas are illuminated in two different configurations, illumination from top (from Au disk side), shown with red arrow and curves, and illumination from bottom (from Ag disk side), shown with green arrow and curves. The nanoantennas with 30 nm spacer show the highest asymmetry in the reflection and absorption spectra between illumination from Au and Ag disks. No asymmetry is observed in transmission. These nanoantennas have bigger Au disks and this asymmetry is caused by absorption in the Au disk. As seen in SEM images, when the spacer thickness increases, nanoantennas become more conical and the Au disk, which is the top disk, becomes smaller. This is a problem behind directional nanoantenna design in this configuration because when Au disks get smaller in volume, plasmonic overlap between Au and Ag disks resonances decreases.

Optical measurements show that the vertical nanoantenna with 30 nm spacer thickness give the best result among all measured nanoantennas. Therefore we continued the next step with 30 nm spacer nanoantennas where we functionalize the nanoantennas with spectrally overlapping quantum dots.
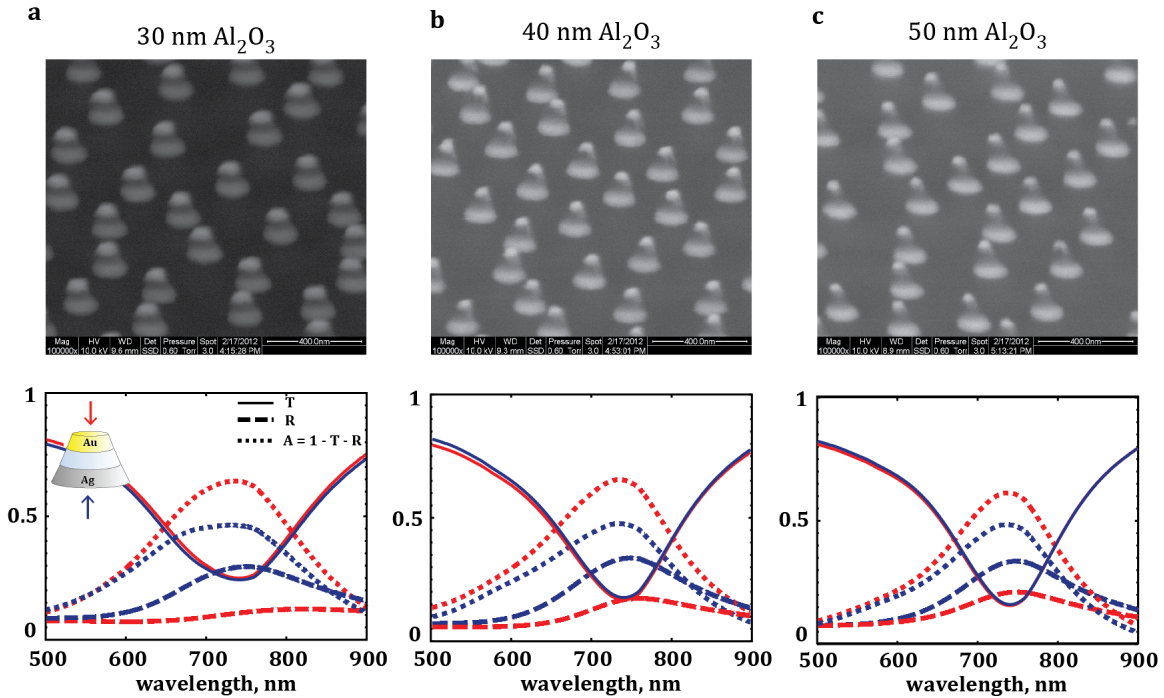
Figure 2.6 - SEM (first row) and optical measurements (second row) for different Al_2O_3 thicknesses (a) 30 nm (b) 40 nm and (c) 50 nm. The red curves show the spectra illuminated from top (Au disk) and the blue curves show the spectra illuminated from bottom (Ag side). The transmission measurements are plotted with continuous lines and the reflection spectra are plotted with big dashed lines. The small dashed lines show the corresponding absorption spectra calculated from the transmission and reflection spectra (A=1-T-R).

The quantum dots are chosen to have their emission peak at 705 nm and they are coated with streptavidin. Nanoantennas are functionalized with biotin and streptavidin biotin interaction is used to attach quantum dots to nanoantennas. The details of the surface functionalization are given in Chapter 5 where experimental methods are described. As shown in Figure 2.7, while quantum dot functionalization of control nanodisks made of only Au successfully show reproducible and uniform fluorescence emission, only Ag nanodisks and bimetallic nanodisks which consist of both Ag and Au did not show any fluorescence emission.

In addition to the vertical configuration, elongated bimetallic nanoantennas are fabricated in the horizontal configuration as well as shown in Figure 2.8 in order to have more freedom to isolate the Ag disk from the Au disk. For this purpose different materials are evaporated only on Ag disks such as Al_2O_3 and palladium. However, this still did not result in homogenous and reproducible fluorescence emission from the nanoantennas in the presence of Ag. The details of the fabrication are given in Chapter 5.

15

only Au disks   only Ag disks
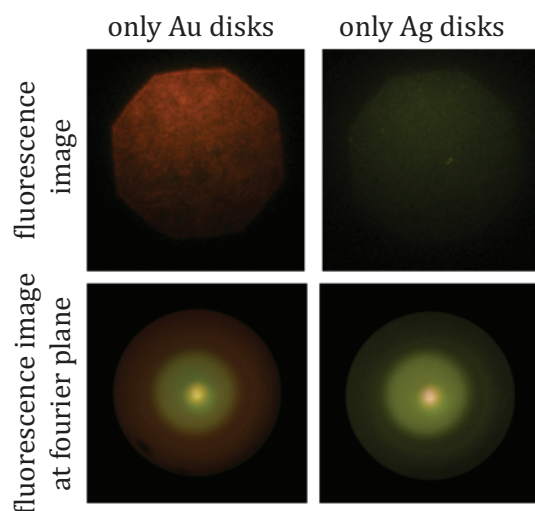
Figure 2.7 – Fluorescence images of control samples consist of only Au and only Ag disks functionalized with 705 nm quantum dots. While Au nanodisks show fluorescence emission from the quantum dots, Ag nanodisks do not.
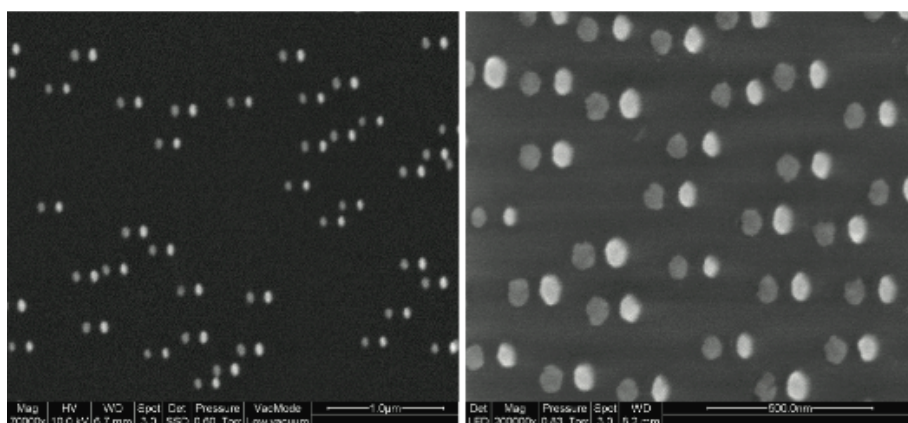
Figure 2.8 – SEM images of elongated bimetallic nanoantennas. The brighter disks are Au and the dimmer ones are Ag particles.

One possible reason for quantum dot attachment failing to function in the presence of Ag, while giving robust, reproducible and uniform immobilization in the presence of only Au, can be due to the Ostwald ripening effect [69]. The Ostwald ripening effect occurs when large particles grow by consuming the particles with small size due to odatoms. It has been also shown that due to this effect Ag atoms can grow on Au surfaces diffusion, ligands, and chemical potential play an important role. Especially thiol molecules, which are used for immobilization of quantum dots on bimetallic nanoatennas, can carry and transport atoms from one particle to another [69], [70].

Before finalizing this chapter, it should be noted that most of the fluorescent

molecules have polarized emission in free-space. The directional emission of fluorescence molecules by plasmonic nanoantennas is still dependent on the original dipole orientation. In order to obtain strong and efficient directional emission, coupling is needed between plasmonic nanoantenna and the molecule [61]. The coupling between emitters and plasmonic nanostructures are described in Chapter 4.

Chapter 3

Molecular Resonances

When a molecule is placed in an optical resonator of volume V that supports several electromagnetic modes, it can emit or absorb a photon by going through transitions between its energy levels. Such interactions can be explained by quantum electrodynamics and in this chapter some key results are discussed. Let us consider an optical resonator which has a mode of frequency $v \approx v_0$ that matches the energy levels of the molecule $hv_0 = E_2 - E_1$. [41].

3.1 Spontaneous emission and absorption

When a molecule is in an excited energy level and decay, the excitation energy can radiate into in the electromagnetic mode as a photon. This process does not depend on the number of photons already present in the mode and is thus called **spontaneous emission** (Figure 3.1 (a)). The decay probability per second, or rate, for this given by:

$$p_{sp} = \frac{c}{V}\sigma(v)$$

(3.1)

where the V is cavity volume, $\sigma(v)$ is the *transition cross section* (cm^2) centered about the atomic frequency v_0 [41].

If the molecule in the cavity is in its ground state and if a photon is available in the cavity, this photon can be taken up by the molecule by raising the molecule to the higher energy level. This process is called **absorption** (Figure 3.1 b)). The probability for absorption is governed by the same law as for spontaneous emission [41].

$$p_{abs} = \frac{c}{V}\sigma(v)$$

(3.2)

Because the process is induced by a photon, the process depends on the number of photons in the cavity. If there are n photons in the cavity, it increases the probability of photon absorbed by the atom n times.

$$P_{abs} = n\frac{c}{V}\sigma(v)$$

(3.3)
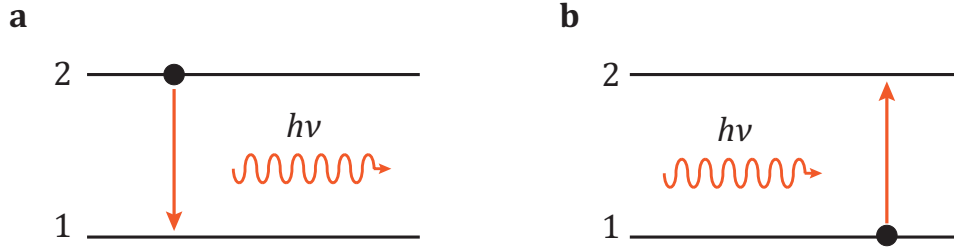
Figure 3.1 – (a) spontaneous emission of a photon into the mode of frequency v by an transition from energy level 2 to energy level 1. (b) absorption of a photon with energy hv leads to upward transition from energy 1 to energy 2. (reproduced from [41])

3.2 The lineshape function

The transition cross-section $\sigma(v)$ described in previous parts characterizes the interaction of the molecule with the field of the mode. The area of the transition cross section describes the strength of this interaction and is called **transition strength** or **oscillator strength**. It has units of cm^2-Hz and is given by the following equation:

$$S = \int_0^\infty \sigma(v)dv$$

(3.4)

The shape of the transition cross-section gives the relative interaction strength for photons with different energies. The normalized function of the transition cross section is called **lineshape function** $g(v) = \sigma(v)/S$ and has units of Hz^{-1} and unity area. The lineshape function is centered at v_0 and the width of the lineshape function is known as **transition linewidth**, which is defined as the full width at half maximum [41].

Absorption and fluoresce spectra of dye molecules in ensemble measurements can show linewidth tens or hundreds of meV at room temperature. For instance, Rhodamine 6G molecule in ethanol has roughly 170 meV [71] and J-aggregate of TDBC molecule can have around 30 meV linewidth at room temperature. Even though the molecules that make the ensemble measurement are chemically identical, since they sense different surroundings, they can have different spectra to a small degree, which results in **inhomogeneous broadening**. When we consider the absorption or fluorescence measurement of a single dye molecule, the spectrum is free of inhomogenous broadening, and it only has **homogenous broadening**. **Lifetime broadening** and **collision broadening** are examples of homogenous broadening. Lifetime broadening can be understood from the Fourier transform of decay of an excited state using an exponential function, $E(t) = E_0 e^{-t/T_1}$ where T_1 is the lifetime of the lowest excited state and E_0 is the initial value of the excited state.

The energy width can be obtained from the Fourier transform of the lifetime function. The real part of the resulting function has a Lorentzian shape:

$$g(v) = \frac{\Delta v/2\pi}{(v - v_0)^2 + \left(\Delta v/2\right)^2} \qquad (3.5)$$

with the following lifetime broadening linewidth

$$\Delta v = \frac{1}{2\pi T_1} \qquad (3.6)$$

While homogenously broadened spectra of a single molecule has Lorentzian lineshape, due to the collective and statistical behavior of molecules, inhomogenously broadened spectra have a Gaussian shape.

3.3 Rayleigh and Raman Scattering

Rayleigh scattering means elastic scattering this is, the photon energy does not change when the photon is scattered (Figure 3.2 (a)). However, the scattered photon changes direction compared to the direction of the incident photon. The intensity of scattering is dependent on the wavelength λ, the number of scatters N, the distance from the scatter R, and polarizability α as expressed in equation 3.7.

$$I = I_0 \frac{8\pi^4 N \alpha^2}{\lambda^4 R^2} (1 + cos^2\theta) \qquad (3.7)$$

Rayleigh scattering occurs if the dimensions of the scatterers are much smaller than the wavelength of the incident light λ_0. If the scatterers is spherical and larger than $\approx \lambda_0/10$, then it is known as **Mie scattering**.

Unlike Rayleigh scattering, **Raman scattering** is an inelastic process for which the energy of the scattered photon changes with respect to the incident photon. The energy difference (hv_R) usually corresponds to a vibrational mode frequency v_R. In Stokes scattering the photon loses its energy (Figure 3.2 (b)) and in anti-Stokes scattering the opposite happens (Figure 3.2 (c)).
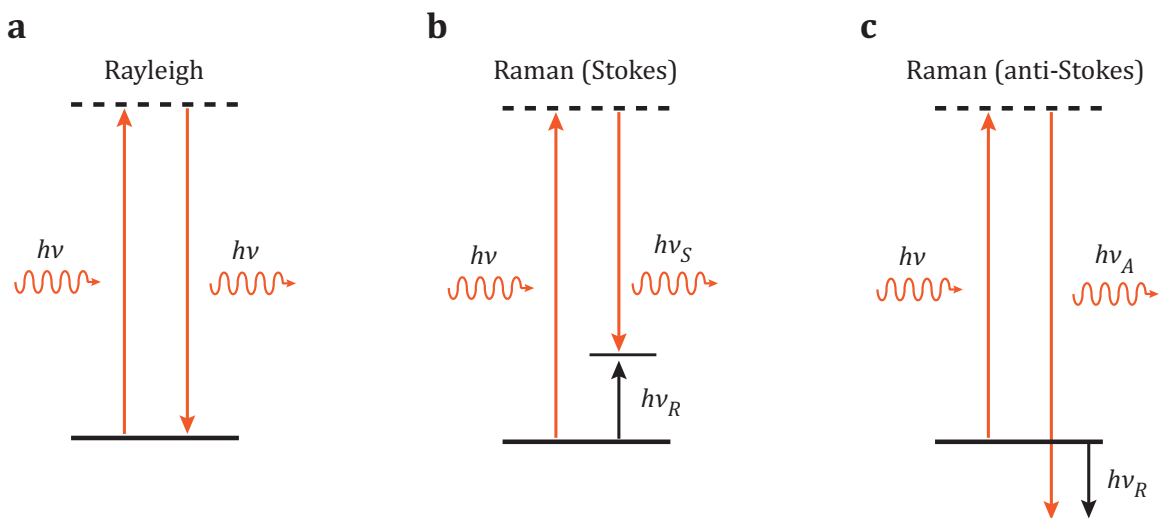
Figure 3.2 – Three different forms of light scattering. (a) Rayleigh. (b) Stokes Raman (c) anti-Stokes Raman. The dashed lines on the top show the virtual states. (Reproduced from [41]).

3.4 Fluorescence

When a molecule is excited from the ground electronic state to a higher electronic state by absorption of a photon, the molecule temporarily stays in its excited state, usually in the range of picoseconds to nanoseconds. This is referred as the fluorescence lifetime. The excitation from the ground state to a vibrationally excited electronic state such as S_1 shown in Figure 3.3 with green arrows happens in the femtoseconds (10^{-15} s) range. Then the molecule can relax to lower S1 state by loosing its energy to the environment. This is called thermal relaxation and takes place in the picoseconds range (10^{-12} s). Thermal relaxation is shown with dark blue lines in Figure 3.3. [72]

Once the molecule is in its vibrationally relaxed state, it can decay into the ground state through different ways. If it decays and emits a photon, this is called fluorescence and usually has a lifetime around nanoseconds (10^{-9}-10^{-6}s). One should note that the intrinsic spontaneous rate of fluorescence is not the measured rate of fluorescence. It is the longest average time that is spent in excited electronic state when no other paths lead to decay to the ground state. It is defined for an isolated molecule and it is the basic quantum mechanical property. Change in the density of photons can alter this intrinsic rate, such as being in the close vicinity of a plasmonic nanoparticle as described in Chapter 4. Any effect that can modify the coupling between the ground and excited states can cause this rate to change, such as molecular conformation fluctuation. Otherwise the rate stays constant [72].

From vibrationally relaxed state S_1 the molecule can also undergo nonradiative relaxation, usually by giving its energy to the environment, which is referred as

internal conversion or thermal relaxation. It is related with the interaction of the molecule with its environment such as solvent, which is depended on temperature and the properties of the solvent. The molecule can couple to its surrounding through vibrations and collusions, referred to as intermolecular coupling. This effect can be observed as broadening of the fluorescence spectrum, such as inhomogeneous broadening. In addition to intermolecular coupling, intramolecular vibrational interactions can also cause molecules to loose energy corresponding to different vibrational levels. This is the main reason for the Stokes shift, which is that the emitted photons energy are lower than the excitation energy [72].

Another possible decay pathway is due to quenching. When the excited molecule collides with dynamic quenchers by random diffusion of the quencher, it can relax to the ground state. Triplet oxygen is one example of a dynamic quencher. They can also increase the rate of transition to triplet states, known as intersystem crossing. The decay rate due to dynamic quenching depends on the concentration of quenchers and the viscosity of the solvent. Plasmonic nanoparticles can also be quenchers. This is described in more detail in Chapter 4 [72].
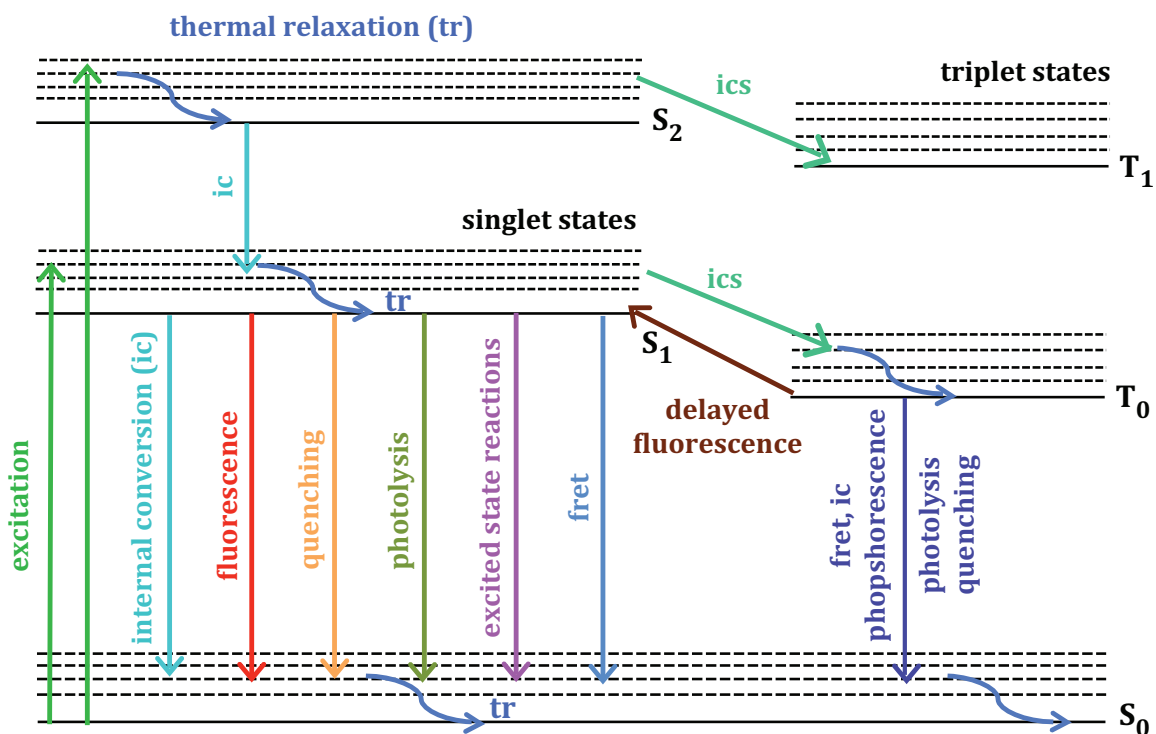
Figure 3.3 – Perrin-Jablonski energy level diagram of a fluorescent molecule. Ics stands for intersystem crossing (Reproduced from [72,73]).

Förster (or Fluorescence) Resonance Energy Transfer (FRET) can be another mechanism for decay of the excited state. This is discussed in more detail in Chapter 4.

Finally, there can be additional pathways for de-excitation, such as photolysis, excited state reactions, intersystem crossing (ics), and delayed emission. These processes are not the subject of the thesis and the attached papers but the details of these processes can be found in [73] and [72].

3.5 Rhodamine 6G (R6G)

R6G, also known as Rhodamine 590, is a fluorescent dye molecule with high stability and high quantum yield. Because of these properties it has been widely used in dye lasers and as a fluorescence tracer in many applications [74]. The chemical structure, 3D geometry, and some parts of the energy level structure of R6G are shown in Figure 3.4.
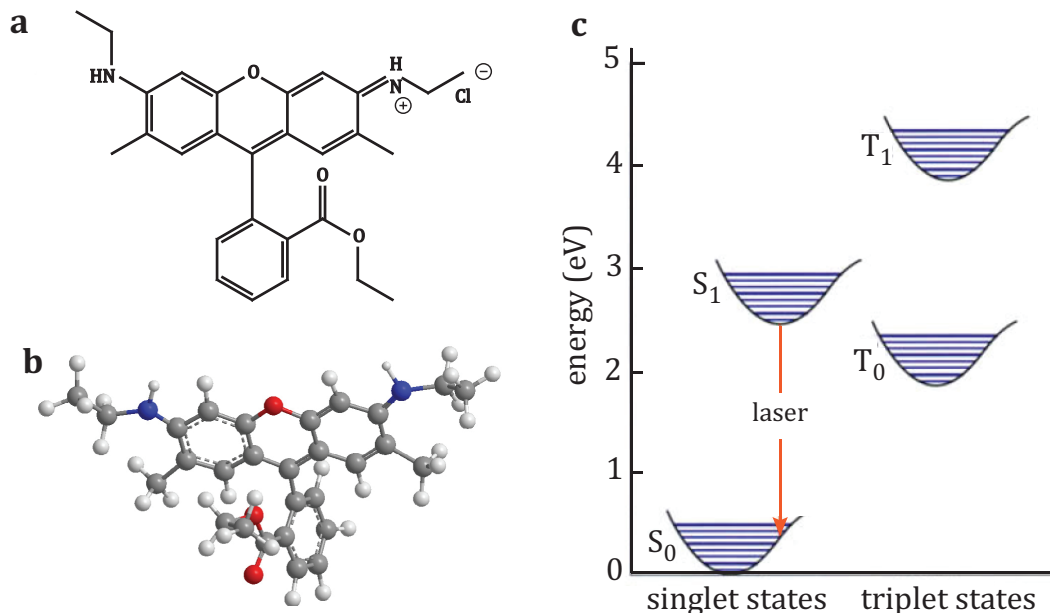
Figure 3.4 – (a) Chemical (b) 3D structure of the R6G ion. (c) Schematic illustration of the partial energy level structure of R6G. Thick and thin lines show vibrational and rotational energy levels respectively (Reproduced from [41,74]).

R6G has also been a widely studied in the context of molecule-plasmon interaction especially with silver nanoparticles for surface enhanced Raman spectroscopy (SERS) ([16,75–80]. The first experimental observation of SERS of R6G adsorbed on colloidal Ag nanoparticles was reported by Hildebrandt and Stockburger [76]. Detection of a single R6G molecule on Ag nanoparticles at room temperature made SERS an important spectroscopy tool for single molecule studies [16,77]. The interaction between R6G and Ag nanoparticles was further investigated by localized

surface plasmon resonance (LSPR) response of the Ag nanoparticles to R6G binding [8,80]. The wavelength shift of the plasmon resonance showed dependency on the spectral overlap between plasmon and molecular resonances due to plasmon-molecule coupling. In Paper 3, we further studied the interaction of R6G with Ag particles where surface enhanced absorption dominates.

3.6 J-aggregates

Molecular aggregates are structures, that show characteristics intermediate between a single molecule and a bulk material. They can consist of ten to thousands of monomer molecules. When the monomers form aggregate structures their optical properties change distinctly and they can show nonlinearites [81,82].

In 1930s, Scheibe and Jelley independently observed this interesting behaviour in pseudoiso-cyanine chloride (PIC). When the concentration of the PIC dye is increased (above around 1 – 10 mM) in aqueous solution, the peak position of absorption of the dye shifted towards higher wavelengths. The full width at half maximum (FWHM) narrows. The absorption coefficient increases, thereby amplifying strong fluorescence emission with a small Stokes shift [83]. Figure 3.5 shows the absorption spectra of PIC chloride aggregates in water (the solid line) and PIC chloride monomers in ethanol (the dashed line). The structure of PIC chloride is shown in the inset.
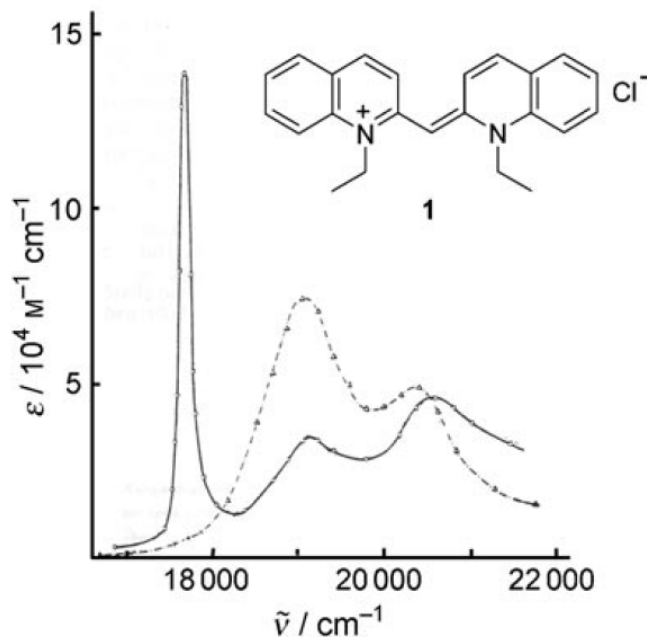
Figure 3.5 - Absorption spectra of PIC chloride monomers in ethanol (dashed line) and aggregates in water (solid line). The inset shows the structure of the PIC molecule [83].

Similar spectral effects were observed in aqueous solutions of the PIC dye upon increasing NaCl concentration, which leads to screening of electrostatic charges and thus promotes aggregation. These spectral changes were interpreted as a result of dye polymerization and are called either Scheibe aggregates or J-aggregates (J denoting Jelley) referring to the name of the discoverers. If the aggregates have absorption bands shifting towards blue wavelengths, they are called H-aggregates (H denoting hypochromic). These aggregates usually show low or no fluorescence emission. Different possible arrangements of the dye molecules in the aggregates, such as brickwork, ladder, or staircase arrangements have been suggested [83]. Among these models, the brickwork arrangement, was considered to be the most likely arrangement of monomers in PIC J-aggregates. Later, a threaded double-string model was proposed, which may be interpreted as a subunit of the brickwork model. Another suggested model was threadlike aggregates composed of two monomers per unit length. Even though the true nature of aggregate molecules is still under investigation, head-to-tail arrangement of monomers to form J-aggregates, the parallel arrangement of monomers to form sandwich type aggregates, H-aggregates, are considered.

Molecular optical theory can provide an explanation as to why the J-aggregates show distinct properties compared to their monomers. Figure 3.6 shows the energy states of inter-molecule coupling for head-to-tail and parallel oriented molecules. When two molecules are close to each other, their transition moments interact to form two new energy states. In Figure 3.6 the dashed lines represent forbidden transitions. According to the molecular exciton theory described in [84], if molecules oriented in the head-to-tail configuration exhibit an in-phase arrangement, the transition dipoles cause an electrostatic attraction and therefore a lower energy state. Similarly, an out-of-phase arrangement leads to electrostatic repulsion and a higher energy state. Consequently, an in-line transition dipole state results in the strong spectral red shift with respect to monomer due to energy lowering. Likewise, electronic transitions in parallel dimers is blue shifted with respect to electronic transitions in monomers. In both head-to-tail and parallel configurations, the in-phase arrangement leads to larger dipole moments and stronger absorption compared to the monomer case.
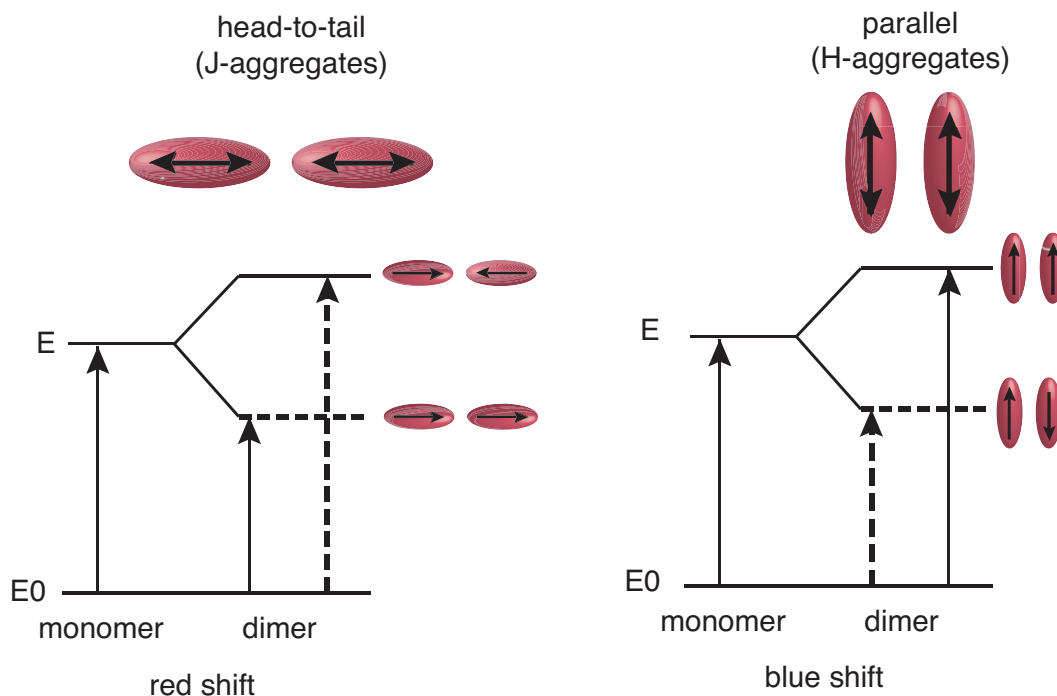
Figure 3.6 Exciton splitting of dimers in different configurations. Orientations of the dipoles are shown by the arrows [84,85].

The McRae Kasha exciton model further states that a red shift in transition can occur when the angle between the transition dipoles and the molecular axis of the aggregate is less than 54 degrees. If the angle is greater, blue-shifted transition occurs as in H-aggregate case [86,87].

Narrowing in the exciton absorption band occurs in addition to the red-shift described above. The origin of the narrowing of the linewidth has been explained by the ultrafast coherent hopping of the excitons, in other words their delocalization [81,88]. While the wave function of a molecular exciton is localized on a single molecule, wave function of the exciton in J-aggregates is extended over many molecules and the number of molecules that the exciton spreads over define describes the size of the exciton [81].

As a result of the delocalization of the exciton, the local inhomogeneities are averaged over and inhomogenously broadened lines become narrower. This results in narrowing of the inhomogeneous linewidth. The narrowing of the linewidth occurs if the intermolecular coupling overcomes the width of the frequency distribution at the different parts. However, common inhomogeneities at different parts cannot be averaged over, therefore there will still be remaining inhomogenous broadening of the linewidth. The linewidth of the J-aggregates depends on the number of molecules participating in exciton delocalization [88]:

$$\frac{\gamma_{monomer}}{\gamma_{Jaggregates}} \propto \sqrt{N} \tag{3.8}$$

Note that the actual physical size of a J-aggregate can be much larger than N though. For instance, the delocalization in J-aggregates of PIC was estimated to be ~4 [87]. In Paper 1 and Paper 2, we used J-aggregates of TDBC. Its monomer and J-aggregate absorption spectra are given in Figure 3.7 with the structure of the monomer in the inset [89]. For TDBC, the exciton delocalization length was estimated to be 16 molecules per J-aggregate at room temperature [82].
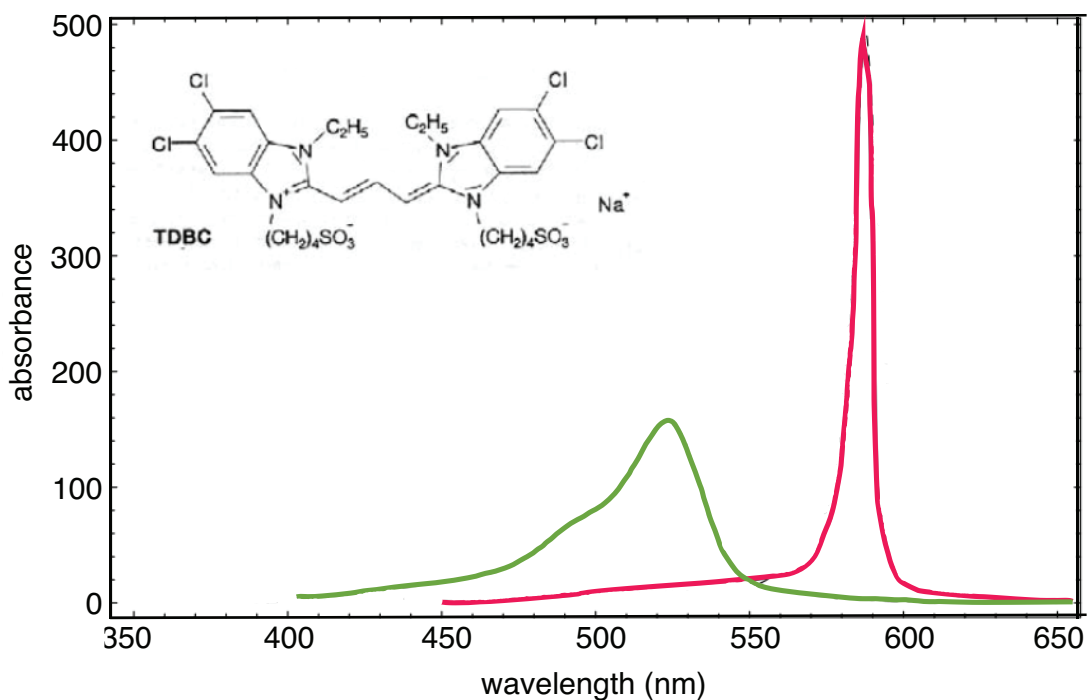
Figure 3.7 The absorption spectra of TDBC dye in monomer (green curve) and J-aggregate (red curve) forms. The inset shows the structure of the dye adapted from [89].

Chapter 4

Molecule-Plasmon Interactions

Plasmon-molecule interactions depend highly on the electronic structure of the molecule and can be categorized into two kinds of interactions: non-resonant and resonant coupling. Non-resonant coupling takes place when the excitation energy of the molecule is not overlapping with the plasmon resonance energy, while resonant coupling occurs in case of a spectral overlap between molecular absorption and plasmon resonance [38]. This chapter will provide the basics of different molecule-plasmon interactions and some examples from my own research.

In non-resonant interactions, the molecular resonances are strongly detuned from the plasmon resonance energy [90]. Thus, these molecules can be considered as being a non-absorbing dielectric medium for the plasmonic nanostructures. Two types of non-resonant coupling are described in this section, namely refractive index dependent plasmon shift and non-resonant surface-enhanced Raman scattering (SERS).

Resonant interactions occur if the molecule exhibits a strong light absorption around the plasmon resonance energy. This interaction can be weak or strong depending on the distance between the plasmonic particle and the molecule, as well as the electronic structure of the two. In this section, the background for several important cases, including, resonant SERS, surface-enhanced fluorescence (SEF), plasmon enhanced FRET, electromagnetically induced transparency, and strong coupling are given. Although not all of these phenomena were studied in this work, they are forming the basis for strong light-matter interactions and therefore are important.

4.1 Refractive index dependent plasmon resonance

By measuring the shift in the plasmon peak position in the extinction spectrum, it is possible to sense different molecules and solvents via refractive index change. Shift in the peak position can be extracted by fitting the plasmon resonance peak to a polynomial function. In Figure 4.1 the consecutive adsorption of different molecules on the same gold nanodisks is shown. The plasmon peak position shift depends on both the molecule and the buffer solution. The gold nanodisks were prepared by hole-mask colloidal lithography, and they are 100 nm in diameter and 30 nm in height. They show a plasmon peak position at around 658 nm in the first buffer. The first injected solution is a mixture of thiolated polyethyleneglycol (PEG) and thiolated polyethyleneglycol biotin (PEG-bio). Thiol covalently binds to the gold

surface, which results in a red shift in a peak position of 8 nm. As buffer 1 is exchanged with buffer 2, that has a lower salt concentration, the plasmon peak position blue shifts 4 nm. The injection of polylysine-graft-polyethyleneglycol (PLL-g-PEG) does not result in a large shift in the plasmon peak position because it binds mainly to the glass substrate. Finally, streptavidin coated quantum dots (SA-QD) are introduced, and these bind to the biotin-adsorbed surface, giving rise to 2.5 nm peak shift.
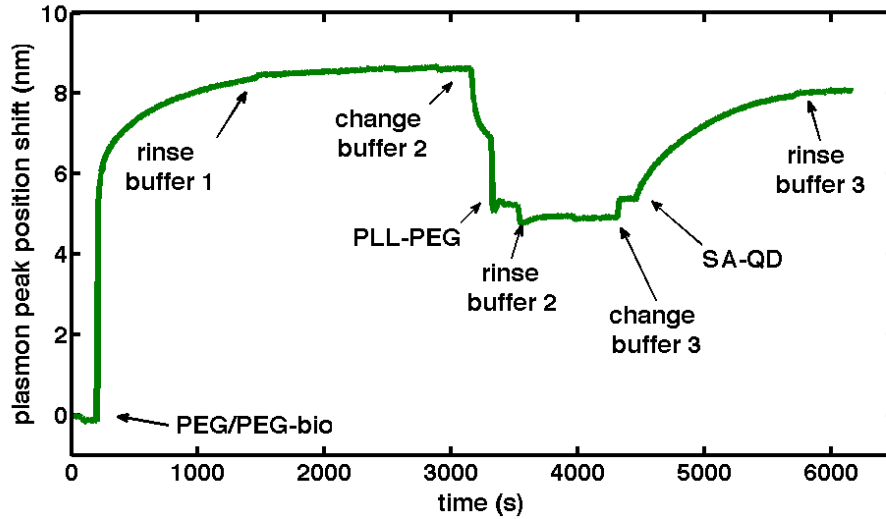
Figure 4.1 - Change in the plasmon peak position by adsorption of different polymers and proteins (PEG/PEG-bio, PLL-g-PEG, SA-QD) on gold nanoparticles in different buffer solutions.

4.2 Surface-enhanced Raman scattering (SERS)

Electromagnetic enhancement of SERS

When a molecule is placed close to a metal nanoparticle, the excitation of a particle surface plasmon greatly increases the local field experienced by the molecule. The nanoparticle does not only enhance the incident field but also the Raman scattering from the molecule, that is, the particle acts as an antenna for the molecule [38].

In the absence of plasmonic nanoparticles, the total Stokes Raman signal from a molecule $P^{RS}(\omega_s)$ is proportional to the Raman cross section of the molecule σ_{free}^R, the excitation laser intensity $I(\omega_s)$, and the number of molecules in the probed volume N [91].

$$P^{RS}(\omega_s) = N\sigma_{free}^R I(\omega_s)$$

$$(4.1)$$

When the molecule is in the vicinity of the metal nanoparticle, experimental observations suggest that the total Stokes Raman signal $P^{SERS}(\omega_s)$ is modified by two effects: the enhancement of local electromagnetic fields, and a chemical enhancement. We express the electromagnetic enhancement factors for the laser and the Raman scattered field as $A(\omega_L)$ and $A(\omega_s)$ respectively (ω_L is the laser frequency and ω_s is the frequency of the Raman scatted field). With chemical enhancement the molecule experiences a different Raman process, described by a new Raman cross-section σ_{ads}^R. The number of molecules involved in the SERS process is N'. The total SERS signal can be written as

$$P^{SERS}(\omega_s) = N'\sigma_{ads}^R |A(\omega_L)|^2 |A(\omega_s)|^2 I(\omega_L)$$

(4.2)

If we consider a small metal sphere in the quasi-static approximation (see Section 2.1), the distribution of the induced electric field E_{sp} of a point dipole in the centre of the metal sphere is given by the following formula. Note that this formula is given for the molecules oriented along the radial direction of the metal sphere.

$$E_{sp} = \frac{\varepsilon_{metal}(\omega) - \varepsilon_{medium}}{\varepsilon_{metal}(\omega) + 2\varepsilon_{medium}} \frac{r^3}{(r+d)^3} E_0$$

(4.3)

molecule

d

r
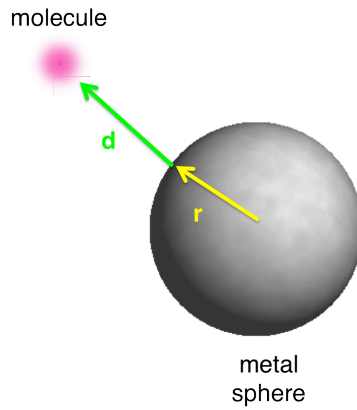
metal
sphere

Figure 4.2 - Schematic diagram for illustration of the concept of electromagnetic SERS enhancement

If the molecule is at a distance d from the surface of the metal sphere, as depicted in Figure 2.2, it experiences the field $E_{molecule}$, which is the superposition of the incident field E_0 and the induced field E_{sp}.

$$E_{molecule} = E_0 + E_{sp}$$

(4.4)

The ratio of the total field at the position of the molecule to the incident field gives the field enhancement factor $A(\omega)$. It is stronger when the excitation of surface plasmons of the metal sphere is resonant.

$$A(\omega) = \frac{E_{molecule}(\omega)}{E_0(\omega)} \sim \frac{\varepsilon_1(\omega) - \varepsilon_2}{\varepsilon_1(\omega) + 2\varepsilon_2} \left(\frac{r}{r+d}\right)^3 \qquad (4.5)$$

The electromagnetic enhancement factor for the total Stokes signal, $G_{em}(\omega_s)$, is

$$G_{em}(\omega_s) = |A(\omega_s)|^2 |A(\omega_L)|^2 \sim \left|\frac{\varepsilon_1(\omega_L) - \varepsilon_2}{\varepsilon_1(\omega_L) + 2\varepsilon_2}\right|^2 \left|\frac{\varepsilon_1(\omega_s) - \varepsilon_2}{\varepsilon_1(\omega_s) + 2\varepsilon_2}\right|^2 \left(\frac{r}{r+d}\right)^{12} \qquad (4.6)$$

From this equation, we can see that the overall enhancement scales with E^4 and it decreases with increasing distance d, as d^{-12}. For single gold and silver nanoparticles, the maximum electromagnetic enhancement is in the order of $10^6 - 10^7$. It is evaluated to be in the order of 10^{11} for the gap between two gold or silver spherical particles separated by 1 nm distance [91].

As described in the previous section, the electromagnetic enhancement of SERS is strong when the excitation and scattered fields are in resonance with the surface plasmons [91]. If the electronic transitions of the molecule are close to laser excitation energy, the signal becomes stronger. This is called surface-enhanced resonance Raman scattering (SERRS) [92].

4.3 Surface-enhanced fluorescence (SEF)

When an isolated molecule (with absorption cross section, σ_{abs}^0) is excited by a laser at energy ω_L and with a photon flux n_L, the total number of absorbed photons is equal to [21]

$$n_{abs}^0 = \sigma_{abs}^0(\omega_L)n_L \qquad (4.7)$$

If an electron is excited from the $S_0(0)$ to the S_1 state and relaxes to the $S_1(0)$ state, then it may radiatively decay to one of the S_0 states, $S_0(\omega_v)$, emitting a photon with a Stokes shift, $\omega_s = \omega_0 - \omega_v$. The total rate for $S_1(0) \rightarrow S_0(\omega_v = \omega_0 - \omega)$ transition is $\gamma_{Tot}^0(\omega_s)d\omega_s$ and the overall decay rate becomes

$$\Gamma_{Tot}^0 = \int \gamma_{Tot}^0(\omega_s)d\omega_s \qquad (4.8)$$

This total rate consists of radiative, $\gamma_{Rad}^0(\omega_s)d\omega_s$ and nonradiative, $\gamma_{NR}^0(\omega_s)d\omega_s$, contributions. The radiative decay rate is

$$\Gamma_{Rad}^0 = \int \gamma_{Rad}^0 (\omega_s) d\omega_s \tag{4.9}$$

The spectral density of radiated power (number of photons per unit time per Stokes frequency) is then given as the following

$$n_{Rad}^0(\omega_s) = \frac{\gamma_{Rad}^0(\omega_s)}{\Gamma_{Tot}^0} \sigma_{abs}^0(\omega_L) n_L \tag{4.10}$$

This fluorescence spectrum of the molecule depends on $\gamma_{Rad}^0(\omega_s)$, which is determined by the density of states $\rho(\omega_0 - \omega_s)$ in the S_0 state. The quantum yield (Q) and the lifetime (τ_0) of an isolated fluorophore are also related to its radiative (Γ_{Rad}^0) and non-radiative decay (k_{nr}) rates [93]

$$Q = \frac{\Gamma_{Rad}^0}{\Gamma_{Rad}^0 + k_{nr}} \tag{4.11}$$

$$\tau_0 = \frac{1}{\Gamma_{Rad}^0 + k_{nr}} \tag{4.12}$$
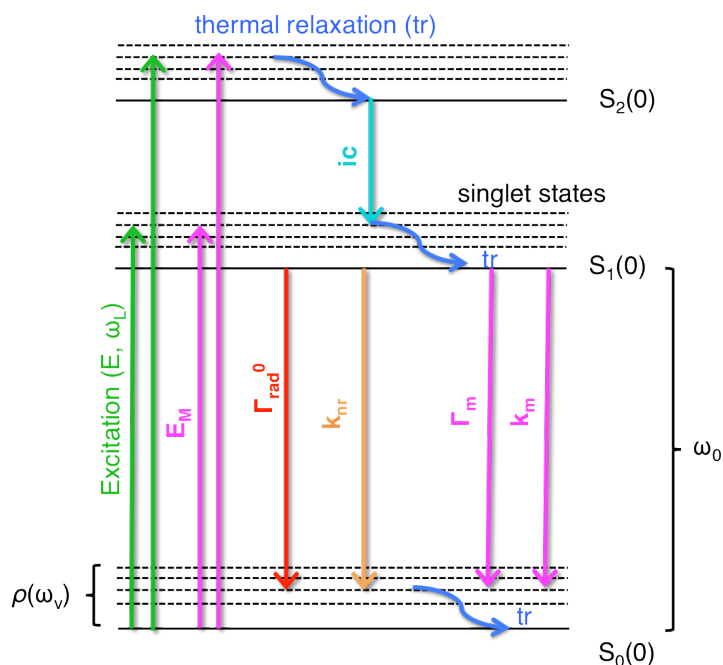
Figure 4.3 - Jablonski energy level diagram of a fluorescent molecule and modifications by nearby metal (shown with pink arrows) [72,93].

In the vicinity of plasmonic metal surfaces, the fluorescence intensity and lifetimes can be modified due to quenching or enhancement by a change in the excitation and emission rates (assuming there is no modification in the molecular energy levels). The excitation rate at the position of the molecule can be modified due to the enhanced local electric field ($E + E_M$). This gives rise to a modification in absorption by a local field enhancement factor $M_{Loc}(\omega_L)$ and changes the brightness of the molecule without affecting the quantum yield or lifetime of the molecule [93]. The emission rate can be altered due to local photonic density of states where factor $M_{Tot}(\omega_s) = M_{Rad}(\omega_s) + M_{NR}$. $M_{NR}(\omega_s)\gamma_{Rad}^0 d\omega_s$ is the decay rate of the emission into the nonradiative channels, such as absorption by the metal, and $M_{Rad}(\omega_s)\gamma_{Rad}^0 d\omega_s$ is the modified radiative decay rate [28]. Additionally, there is an intrinsic nonradiative rate $\gamma_{NR}^0 d\omega_s$, but this is negligible with respect to $M_{NR}(\omega_s)\gamma_{Rad}^0 d\omega_s$. Consequently, the modified overall decay rate for $S_1(0) \rightarrow S_0(\omega_v = \omega_0 - \omega)$ becomes

$$\Gamma_{Tot} = \int M_{Tot}(\omega_s)\gamma_{Rad}^0(\omega_s)d\omega_s = \bar{M}_{Tot}\Gamma_{Rad}^0 \qquad (4.13)$$

and the modified spectral density of radiated power is

$$n_{Rad}(\omega_s) = \frac{M_{Rad}(\omega_s)\gamma_{Rad}^0(\omega_s)}{\Gamma_{Tot}}M_{Loc}(\omega_L)\sigma_{abs}^0(\omega_L)n_L \qquad (4.14)$$

Then, the fluorescence spectral enhancement factor can be written as

$$M_{Fluo}(\omega_s) = \frac{n_{Rad}(\omega_s)}{n_{Rad}^0(\omega_s)} = \frac{M_{Rad}(\omega_s)}{\bar{M}_{Tot}}M_{Loc}(\omega_L) \qquad (4.15)$$

where $M_{Rad}(\omega_s)$ represents the resonance due to localized surface plasmons, which enables strong fluorescence enhancement with overlapping plasmon resonance and fluorescence emission.

The quantum yield, Q_m, and the lifetime of the molecule, τ_m, are also modified as follows:

$$Q_m = \frac{\Gamma_{Rad}^0 + \Gamma_m}{\Gamma_{Rad}^0 + \Gamma_m + k_{nr} + k_m} \qquad (4.16)$$

$$\tau_m = \frac{1}{\Gamma_{Rad}^0 + \Gamma_m + k_{nr} + k_m} \qquad (4.17)$$

As illustrated in Figure 2.3, Γ_m is the additional radiative and k_m is the additional non-radiative decay rate due to plasmonic nanostructure. An increase in radiative rates results in increased quantum yields and decreased lifetimes.

4.4 Purcell Effect

The lifetime of the excited state of an emitter is not an intrinsic property. According to Fermi's golden rule, the spontaneous emission of an emitter depends on the electromagnetic environment through local density of photonic states (LDOS) [94]. The spontaneous decay rate of an emitter can be modified by placing the emitter inside an optical cavity and thus changing its surrounding LDOS [95–97]. This phenomenon is known as the Purcell effect [95]. The enhancement of the spontaneous decay rate of an emitter is described by the Purcell factor as follows [9,97–99]:

$$F_p = \frac{\gamma_{cavity}}{\gamma_{free\ space}} = \frac{3Q\lambda^3}{4\pi^2 n^3 V_{eff}}$$
(4.18)

γ_{cavity} and $\gamma_{free\ space}$ are the decay rates of the emitter with and without the presence of the cavity. Q is the quality factor and V_{eff} is the mode volume described in Chapter 2. λ/n is the wavelength of the light in the material. In other words, the Purcell factor relates the LDOS to the ratio of Q to V_{eff} ($F_p \sim Q/V_{eff}$) and the LDOS can be computed from the imaginary part of electromagnetic Green tensor [100].

4.5 Plasmon enhanced FRET

Another example of molecule-plasmon interaction is plasmon enhanced Förster (alternatively, fluorescence) resonance energy transfer (FRET), where the near-field plasmon resonance of metal nanostructures can couple to molecules in the vicinity. FRET is a nonradiative energy transfer from a donor molecule in the excited state to an acceptor molecule in the ground state through dipole–dipole interaction. FRET is limited to a certain distance between the donor and the acceptor molecules (around 0.5 - 10 nm). Therefore, the FRET efficiency is highly dependent on the donor-acceptor separation distance. The rate of energy transfer between the two fluorophores, k_{FRET}, is determined by the fluorescence lifetime of the donor without the acceptor, $1/\tau_D^{-A}$, the distance between the fluorophores, R, and the characteristic distance, R_0 [72].

$$k_{FRET} = \frac{1}{\tau_D^{-A}}\left(\frac{R_0}{R}\right)^6$$
(4.19)

The characteristic Förster distance is defined as the separation between the donor and the acceptor when the FRET efficiency is 50%. It is proportional to the spectral overlap integral of the donor emission spectrum with the acceptor absorption

spectrum, J, the quantum yield of the donor in the absence of the acceptor, Q_0, the dipole orientation factor, κ^2, the refractive index of the medium, n, and Avogadro number, N_A.

$$R_0^6 = \frac{9Q_0 \ln(10)\,\kappa^2 J}{128\pi^5 n^4 N_A} \tag{4.20}$$

The spectral overlap integral equation, contains contributions of the donor's emission spectrum, $f_{D,em}$, and the acceptor absorption spectrum, $f_{A,abs}$.

$$J = \int f_{D,em}(\lambda) f_{A,abs}(\lambda) \lambda^4 d\lambda \tag{4.21}$$

The FRET efficiency (the quantum yield of the energy transfer) is defined as the ratio of the rate of FRET to the total rate of de-excitation. $1/\tau_D^{+A}$ is the fluorescence lifetime of the donor in the presence of the acceptor.

$$E_{FRET} = 1 - \frac{1/\tau_D^{-A}}{1/\tau_D^{+A}} = \frac{k_{FRET}}{1/\tau_D^{+A}} = \frac{1}{1 + \left(\frac{R}{R_0}\right)^6} \tag{4.22}$$

In an early theoretical work, the energy transfer between two molecules was investigated when the molecules are placed close to a small solid particle [101]. It was shown that FRET could be enhanced with the assistance of the particle in the transfer process. In the presence of the particle, donor dipole induces multipole moments on the particle, which can be much larger than the donor dipole itself. The degree of enhancement of the dipole depends on the shape of the particle, the location of the molecular dipole with respect to the particle, and the spectral match between the plasmon resonance, and the 'overlap integral J'. Firstly, when the particle dipole is excited, it can couple to the acceptor dipole and modify the energy transfer. Secondly, the presence of the particle introduces new decay channels competing with the energy transfer. Hence, the presence of the particle modifies not only the energy transfer rate, but also the radiative and non-radiative decay rates of the donor and acceptor molecules. From the given parameters above, we know that the quantum yield of the donor and the absorption coefficient of the acceptor should be high enough for a significant probability of the transfer, which only takes place in a limited distance between the fluorophores [72]. Plasmonic nanostructures have the potential to enhance the characteristic Förster distance by improving the quantum yield of the donor and the excitation of the acceptor [102].

Figure 4.5 shows some of our preliminary results of enhancing FRET and/or acceptor emission by using plasmonic nanostructures for the ratiometric FRET imaging in mammalian cells. MT1-MMP (membrane type 1 matrix

metaloproteinase) is a membrane-anchored enzyme, known to be crucial during cancer invasion and metastasis. It is observed in a broad range of human cancers in clinical examples. MT1-MMP is tagged by orange and red fluorescent proteins in order to have simultaneous visualization of a MT1-MMP in addition to another FRET biosensor which is tagged by the most commonly used FRET pair cyan-yellow fluorescent proteins [103]. Figure 2.4 gives the schematic diagram of the FRET sensor and both absorption and emission spectra of donor and acceptor fluorescent molecules.
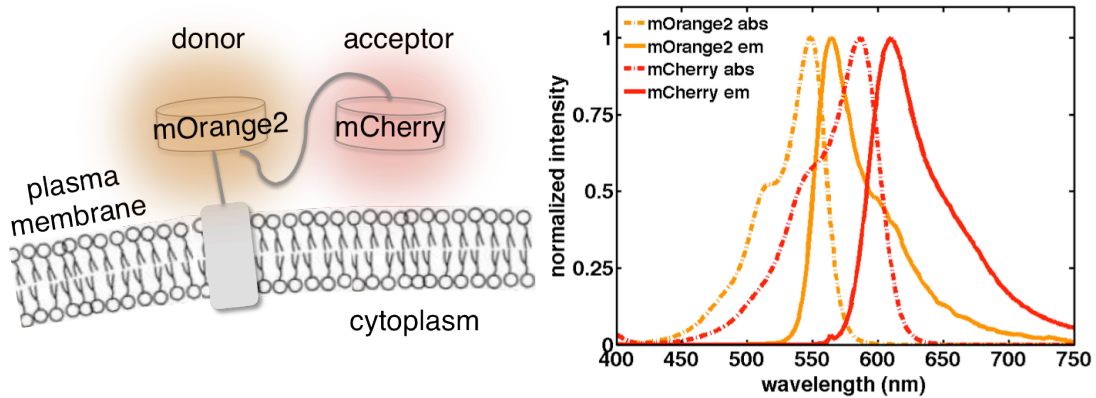
Figure 4.4 - On the left is a schematic diagram of the FRET biosensor. The absorption (dashed lines) and emission (solid lines) spectra of donor (mOrange2) and acceptor (mCherry) fluorescent proteins are shown in the graph. Intensities are normalized [103].

In this system, the acceptor molecule, (mCherry) exhibits quite a low quantum yield, of 0.2. This makes the pair inefficient for ratiometric FRET imaging, a widely used method to measure FRET in biological applications. It is based on separate imaging of the donor and acceptor channels, and subsequent division of one channel by the other to generate the ratio image. In our case, the acceptor channel is divided by the donor channel as shown in Figure 2.5.
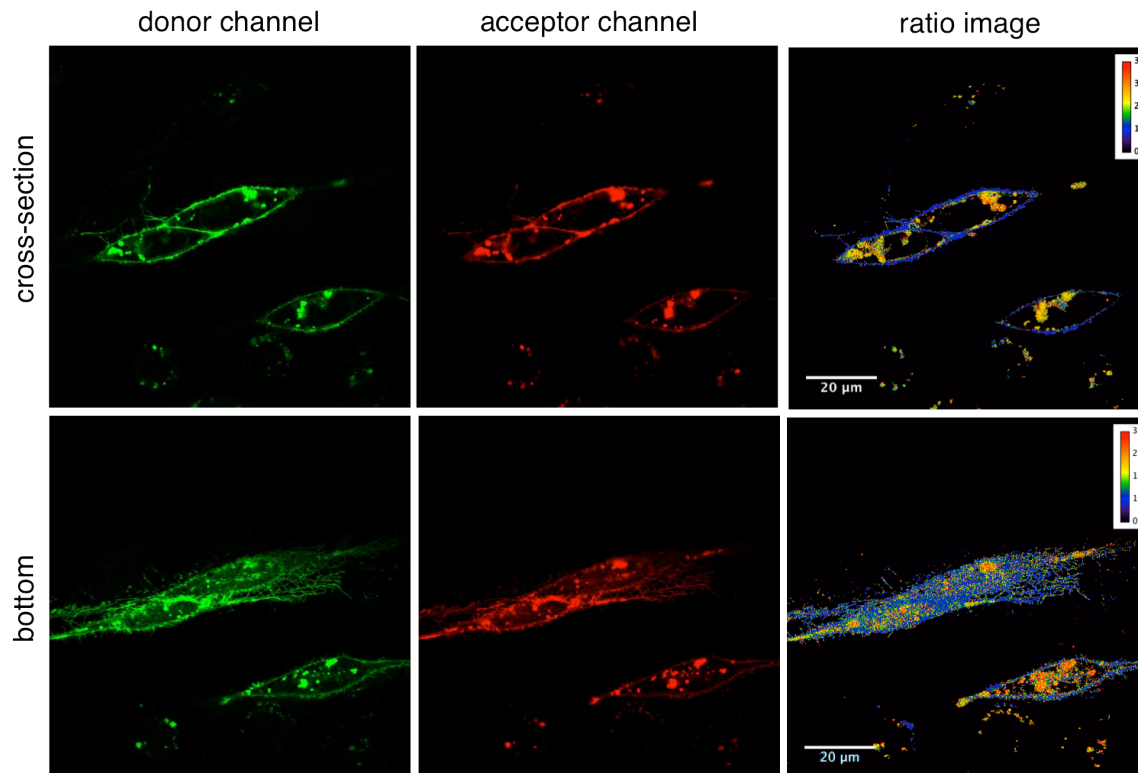
Figure 4.5 - Confocal microscopy images of live HeLa cells expressing the MT1-MMP FRET biosensor on a cover glass. The images in the first row show the cross-section of the two attached cells and the images in the second row show the bottom part of the plasma membrane. The green images are from the donor channel, the red images are from the acceptor channel, and the last column images are ratio images (acceptor/donor).

Our aim was to improve ratiometric imaging by using plasmonic nanoparticles. Figure 4.6 shows the concept our experiments. HEK293 (Human Embryonic Kidney 293) cells expressing the MT1-MMP biosensor are grown on three different plasmonic substrates. Substrate 1 is tuned in such way that the plasmon resonance peak matches the donor emission and the acceptor absorption. Substrate 2 is designed such that the plasmon peak overlaps the emission of the acceptor. The other substrate is the control, a simple cover glass without any particles. For each substrate, 20-25 fluorescence images were collected under the same imaging conditions and parameters. Ratio images were processed according to the described algorithm [104]. The integrated intensity was calculated for each image, and then averaged for the total number of images, giving the averaged integrated intensity. Preliminary results of the experiment are shown in Figure 4.7. Substrate 1 shows a higher intensity in ratio images compared to the control substrate. This substrate led to a higher intensity in the acceptor channel and a lower intensity in the donor channel, possibly due to enhanced energy transfer. However, more experiments are needed in order to analyze the results more quantitatively (e.g. calculate the transfer efficiencies) and to understand the mechanism behind these results.
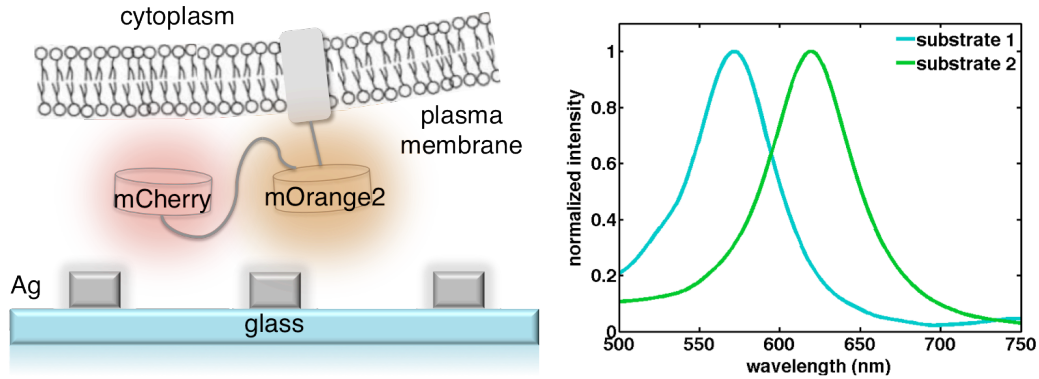
Figure 4.6 - On the left, a schematic diagram showing the mammalian cells expressing the FRET biosensor on the substrates. On the right, normalized absorption spectra of two different substrates measured in water. Substrate 1 exhibits the plasmon peak at 572 nm, overlapping with donor emission and acceptor absorption spectra. The substrate 2 shows a plasmon peak at 620 nm, that overlaps with the acceptor emission spectrum.
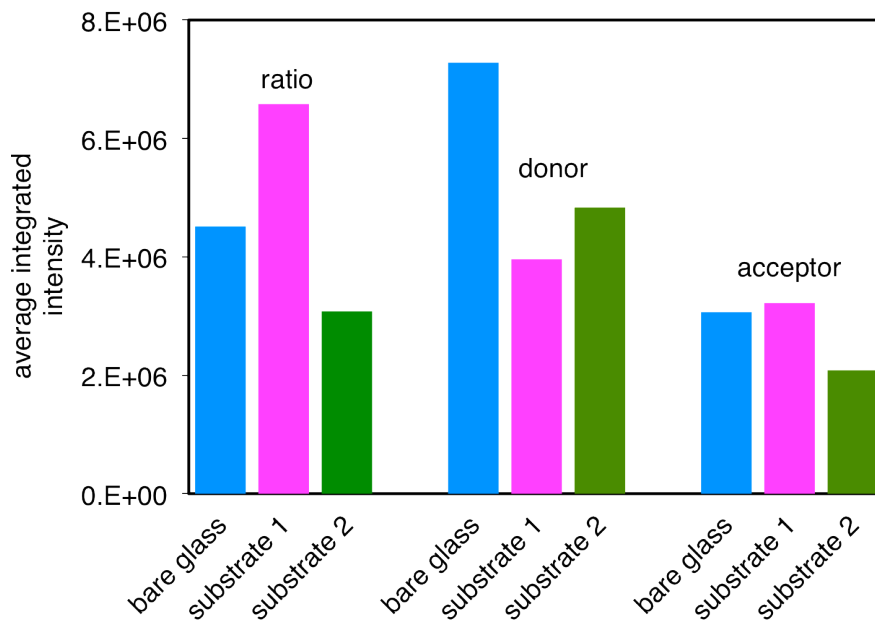
Figure 4.7 - Chart showing the average integrated intensities for different substrates for the donor, acceptor, and ratio images. For each substrate, the integrated intensity was calculated from single cell images and averaged for 20-25 cell images.

4.6 Strong coupling

Strong coupling between molecules and plasmons has been interpreted from many different perspectives. Therefore, it is possible to come across a wide range of terminologies to explain the phenomenon, such as hybridization, plasmon splitting, electromagnetically induced transparency, and plasmon resonance energy transfer. According to Halas et al. [105], when a quantum emitter is placed near a plasmonic nanostructure, the electromagnetic interaction between the surface plasmon and the exciton can result in hybridized states. The wavefunctions of these hybridized states are interpreted as the combination of the exciton and the plasmon mode, and the states are made up of bonding and antibonding states.

According to other authors, the strong coupling can be described as energy transfer between the molecule and the plasmon [106]. For instance, Förster resonant energy transfer (FRET) is considered as a weak coupling between donor and acceptor molecules. FRET assumes that the transfer rate from donor to acceptor is smaller than the relaxation rate of the acceptor, so that once the energy is transferred to the acceptor, there is little possibility of reverse transfer to the donor. When the interaction energy becomes large enough, a reverse transfer to the donor becomes possible, and the system shifts into the strong coupling regime. In this regime, donor and acceptor become indistinguishable, and the molecule-plasmon pair is considered as one system. In a similar manner, plasmon resonance energy transfer (PRET) between plasmonic nanostructures and molecules is another interpretation of strong coupling [18]. By analogy with FRET, where the donor emission and acceptor absorption has to overlap in energy, for PRET a match between the plasmon resonance and the electron transition energy of the molecule is needed, and energy can be transferred through the dipole-dipole interaction between the resonating plasmon dipole and the molecular dipole.

Plasmonic splitting is another perspective in strong coupling literature, which is observed as two or more resonance peaks in the spectrum of the particle, depending on the number of the absorption bands of the molecule [107]. It is considered as an analogy to Rabi splitting in quantum mechanical systems. From this point of view, the plasmonic splitting takes place because of an exchange of photons between the plasmonic nanoparticle and the dye molecules. Such a mechanism under some circumstances can dominate decoherence rates and thus result in new coherent hybrid states.

It was also claimed that by varying the oscillator strength and molecular transition line width, either plasmonic splitting or a quenching of dips could be observed on the spectrum of dye molecule coated plasmonic nanoparticles [107]. According to the authors, the plasmonic energy transfer described by quenching dips at the position of the molecular absorption band occurs when both the oscillator strength and the line width of the molecular transition of the dye are small. For a large line width, overall quenching can be observed. On the other hand, the plasmonic

splitting occurs when both the oscillator strength and line width of the molecular transition of the dye are large.

Energy level splitting is considered as a characteristic feature of the strong coupling interaction and can be understood from a classical approach [106].

4.7 Classical coupled harmonic oscillator model

The coupled harmonic oscillators model is an intuitive classical model used to explain interaction and coupling between a plasmonic nanoparticle and an emitter. Here, the surface plasmon resonance and molecular transition are each treated as damped harmonic oscillators, which represent the polarization of the metal nanoparticles and the emitter [108]. The oscillators are coupled to each other through the electric near field with the coupling strength g and the equations of motion are given as [109]:

$$\ddot{x}_{SP}(t) + \gamma_{SP}\,\dot{x}_{SP}(t) + \omega_{SP}^2\,x_{SP}(t) + g\dot{x}_E(t) = F_{SP}(t) \qquad (4.23)$$

$$\ddot{x}_E(t) + \gamma_E\,\dot{x}_E(t) + \omega_E^2\,x_E(t) - g\dot{x}_{SP}(t) = F_E(t) \qquad (4.24)$$

In these equations x_{SP} and x_E are the coordinates of the surface-plasmon and emitter oscillations, ω_{SP} and ω_E the centre frequencies, γ_{SP} and γ_E are the linewidths, and F_{SP} and F_E are the driving normalized forces because of the external electromagnetic field. The emitter excitation by itself is insignificant with respect to the metal nanostructures, therefore the driving force for the emitter can be ignored. If the applied light has the frequency ω and the driving force is $F_{SP}(t) = \text{Re}(F_{SP}\,e^{-i\omega t})$, the steady state coordinates are expressed as the following:

$$x_{SP}(t) = Re\left(\frac{(\omega_E^2 - \omega^2 - i\gamma_E\omega)F_{SP}(t)}{(\omega^2 - \omega_{SP}^2 + i\gamma_{SP}\omega)(\omega^2 - \omega_E^2 + i\gamma_E\omega) - \omega^2 g^2}\right) \qquad (4.25)$$

$$x_E(t) = Re\left(\frac{-ig\omega F_{SP}(t)}{(\omega^2 - \omega_{SP}^2 + i\gamma_{SP}\omega)(\omega^2 - \omega_E^2 + i\gamma_E\omega) - \omega^2 g^2}\right) \qquad (4.26)$$

The total extinction cross-section of structure, C_{ext}, including both absorption and scattering can be calculated from the work done by the applied force.

$$C_{ext}(\omega) \propto \langle F_{SP}(t)\dot{x}_{SP}(t)\rangle \qquad (4.27)$$

$$C_{ext}(\omega) \propto \omega\,Im\left(\frac{(\omega_E^2 - \omega^2 - i\gamma_E\omega)}{(\omega^2 - \omega_{SP}^2 + i\gamma_{SP}\omega)(\omega^2 - \omega_E^2 + i\gamma_E\omega) - \omega^2 g^2}\right) \qquad (4.28)$$

Even though the scattering cross-section cannot not be calculated in a straightforward way by the coupled-oscillator model, it is still possible to calculate it in quasi-static limit where $k = \frac{\omega n}{c}$ is the wavevector of light and α is the polarizability of the plasmonic nanostructure.

$$C_{ext}(\omega) = 4\pi k Im(\alpha) \qquad (4.29)$$

By using these two equations, the scattering cross-section can be written as

$$C_{sca}(\omega) = \frac{8\pi}{3} k^4 |\alpha|^2 \qquad (4.30)$$

$$C_{sca}(\omega) \propto \omega^4 \left| \frac{(\omega_E^2 - \omega^2 - i\gamma_E \omega)}{(\omega^2 - \omega_{SP}^2 + i\gamma_{SP}\omega)(\omega^2 - \omega_E^2 + i\gamma_E\omega) - \omega^2 g^2} \right|^2 \qquad (4.31)$$

It is also possible to couple the oscillators through linear terms rather than the derivative terms [106,108,110]. This would mean that coupling occurs through displacement rather than velocity and represent a simplified version of the coupling. In that case the equations will be as following:

$$\ddot{x}_{SP}(t) + \gamma_{SP}\,\dot{x}_{SP}(t) + \omega_{SP}^2\,x_{SP}(t) + g\big(x_{SP}(t) - x_E(t)\big) = F_{SP}(t) \qquad (4.32)$$

$$\ddot{x}_E(t) + \gamma_E\,\dot{x}_E(t) + \omega_E^2\,x_E(t) + g\big(x_E(t) - x_{SP}(t)\big) = F_E(t) \qquad (4.33)$$

$$x_{SP}(t) = Re\left(\frac{(\omega_E^2 + g - \omega^2 - i\gamma_E\omega)F_{SP}(t)}{(\omega^2 - \omega_{SP}^2 - g + i\gamma_{SP}\omega)(\omega^2 - \omega_E^2 - g + i\gamma_E\omega) - g^2}\right) \qquad (4.34)$$

$$x_E(t) = Re\left(\frac{gF_{SP}(t)}{(\omega^2 - \omega_{SP}^2 - g + i\gamma_{SP}\omega)(\omega^2 - \omega_E^2 - g + i\gamma_E\omega) - g^2}\right) \qquad (4.35)$$

$$C_{sca}(\omega) \propto \omega^4 \left| \frac{(\omega_E^2 + g - \omega^2 - i\gamma_E\omega)F_{SP}(t)}{(\omega^2 - \omega_{SP}^2 - g + i\gamma_{SP}\omega)(\omega^2 - \omega_E^2 - g + i\gamma_E\omega) - g^2} \right|^2 \qquad (4.36)$$

It has been reported that calculations performed with coupling through both derivate and linear terms resulted in qualitatively similar results in terms of extinction and scattering spectra [109]. We preferred to use coupling through derivative terms in the attached papers because it is intuitively easier to understand; coupling strength being a rate that competes with other damping rates [111].

Figure 4.8 shows the scattering spectra of two coupled harmonic oscillators calculated with equation 4.31. Plasmon resonance is represented by 2.11 eV central frequency and 250 meV linewidth. The molecular resonance has the same central frequency 2.11 eV and linewidth 100 meV. Coupling strength is then tuned from 0 to 1.4 γ_{pl} (350 meV). As the coupling strength g increases, so does the transparency in the scattering spectra. When the coupling strength, g, becomes bigger than the plasmon linewidth γ_{pl}, the excitation energy oscillates between the emitter and the plasmonic nanoparticle. In this case the system enters a truly strong coupling regime. Interaction regimes are explained in more detail the next section.
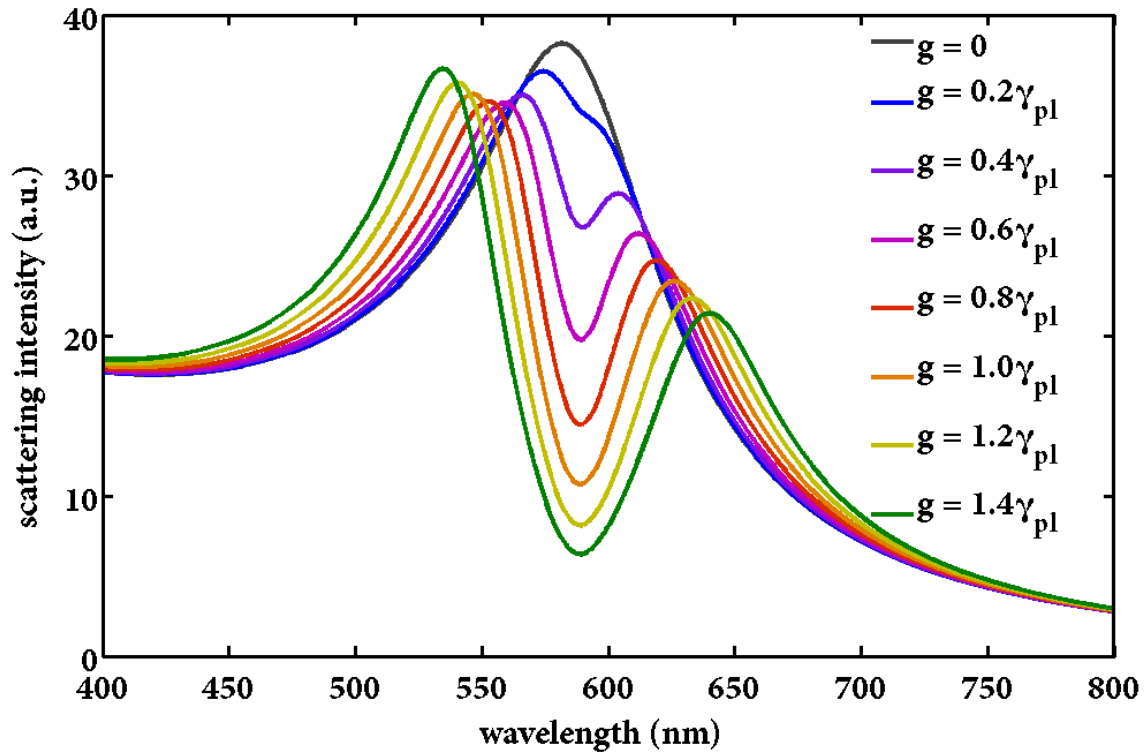
Figure 4.8 - Scattering spectra of two resonators coupled with harmonic oscillator model. In this model, both plasmon and molecular resonance are taken as 2.11 eV (588 nm), with zero detuning. Plasmon and molecular linewidths are set to 250 meV and 100 meV respectively.

4.7 The coupling constant

The coupling constant or strength of the interaction, g, can be also written as:

$$g = \sqrt{N}\mu|E_V| \qquad (4.37)$$

In the equation 4.37, N is the number of emitters interacting with the cavity, μ is the transition dipole moment of the emitter, and E_V is the vacuum field.

$$E_V(r) = \sqrt{\frac{\hbar\omega}{2\varepsilon_0\varepsilon V_{eff}}} \qquad (4.38)$$

Coupling strength and vacuum field can be described within so-called cavity quantum electrodynamics (cQED) framework – a theory that describes interaction of a single two-level atom with a quantized electromagnetic field in an optical cavity [112,113]. According to this model, the total Hamiltonian $\hat{H}$, also known as Jaynes-Cummings Hamiltonian, is given by:

$$\hat{H} = \hat{H}_A + \hat{H}_F + \hat{H}_{int} \qquad (4.39)$$

Where $\hat{H}_A$ is the Hamiltonian of an atom, $\hat{H}_F$ is the Hamiltonian of a single-mode cavity field, and $\hat{H}_{int}$ is the Hamiltonian of the interaction. The complete derivation of Jaynes-Cummings model can be found in the following reference [113].

In CQED, interactions between plasmons and emitters can be classified into two main regimes: the weak coupling regime and the strong coupling regime. The regime of the interaction is determined by relative strength of g to the damping rates of both the cavity γ_{pl} and the emitter γ_0. The weak coupling regime holds when $g \ll \gamma_{pl}, \gamma_0$, and the strong coupling regime holds when $g \gg \gamma_{pl}, \gamma_0$ [112].

In the weak-coupling regime, the damping rates of the emitter and the cavity are larger than the coupling strength, and therefore the excitation in the system irreversibly dissipates before any coherent energy exchange can take place between the emitter and the cavity. In this case, the interaction still affects the emitter and is observed as a modification of the decay rate of the emitter, which is precisely the Purcell effect, as described in the previous section [9].

On the other hand, in the strong-coupling regime the coupling strength is larger than damping rates of both the emitter and the cavity. Therefore, the excitation energy conserved within the system and is reversibly exchanged between the emitter and the cavity, known as Rabi oscillations [114]. This can be also considered, because the excited emitter emits a single photon into the cavity mode and periodically reabsorbs and remits the photon before the excitation decays [112]. These oscillations lead to hybridization of energy levels of the cavity and the emitter [115]. The energy eigenstates of the system, which are often referred to as the dressed states are shown in Figure 4.9. The energy difference between two states is equal to $2g$ [113]. When the coupling between the oscillators strengthens, the energy separation (energy splitting) increases. This can be considered as repulsion between the energies, as the lower energy decreases and the higher energy increases, and is referred to as anti-crossing behavior. This anticrossing in energy with a separation is known as vacuum-Rabi splitting [60].

In Figure 4.9 the energy level diagram for n photons in the cavity, known as the Jaynes-Cummings ladder is also shown [31]. Note that the energy difference between dressed and undressed energy levels is given by $g\sqrt{n}$ for n photons [9].
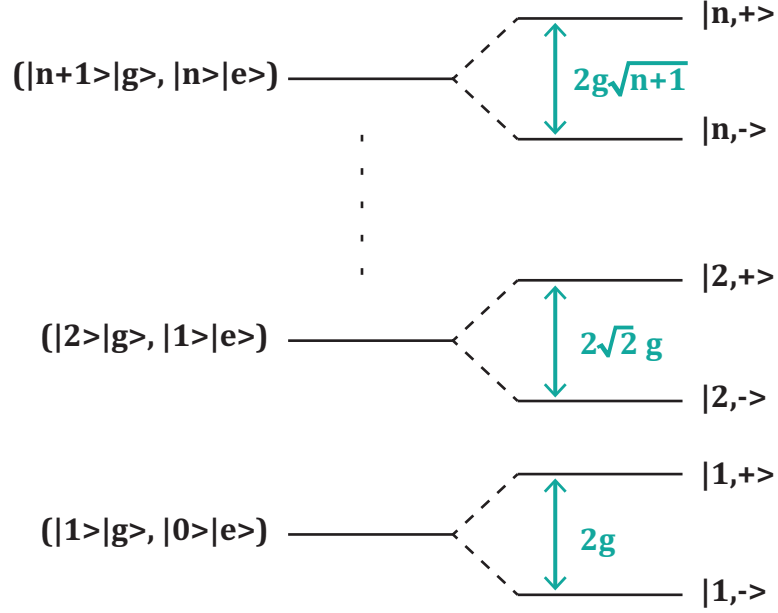
Figure 4.9. The schematic of the dressed energy levels of the Jaynes-Cummings interaction is shown. On the left the degenerate states for no interaction (undressed energy levels) are given [9,113].

In general, it is not easy to reach the strong coupling regime using plasmons, since they are highly lossy. However, an intermediate regime, i.e. $\gamma_{pl} > g > \gamma_0$ can be satisfied fairly easily. This regime is known as the bad cavity limit. Electromagnetically induced transparency is an example of this limit [9,109,116,117].

Because the decay rate of the plasmonic nanoparticles is often the limiting parameter for reaching the strong coupling regime, g/γ_{pl} ratio becomes an important parameter to be maximized. By using the equation 4.37, g/γ_{pl} can be written as following. Here, the ratio depends on the quality factor Q, effective mode volume of the cavity V_{eff} and number of molecules N interacting with the cavity.

$$\frac{g}{\gamma_{pl}} \sim \sqrt{\frac{N}{V_{eff}}}\, Q \tag{4.43}$$

In order to be able to enter the strong coupling regime, the quality factor of the cavity should be increased. This can be done by either reducing the damping of the material or building hybrid cavity systems, e.g., microtoroid resonators and metal

nanoparticle cavities [118] or a plasmon distributed Bragg reflector resonator [119]. These plasmonic hybrid resonators combine the benefits of a high Q-factor and with a small mode volume [9]. Figure 4.10 shows the comparison of different cavities coupled with different emitters [60].

Cavity	Length = 42.2 µm Width = 23.4 µm	Photonic Crystal Slab	Micropillar	Microdisk	Ag Nanotriangle
λ (nm)	852.4	1182	937	744	589
E (eV)	1.45	1.32	1.32	1.66	2.11
Q	4.4×10^7	6000	7350	12000	5 - 20
V (μm^3)	18148	0.04	0.3	0.07	0.4×10^{-6} - 1.4×10^{-6}
F_p	114	441	36	125	8×10^4 - 6×10^5
$\kappa\pi/2$ (meV)	3.3×10^{-5}	0.22	0.18	0.14	106 - 422
Oscillator	trapped Cs atom	InAs QD	$In_{0.3}Ga_{0.7}As$ QD	GaAs QD	J-aggregate
Size	d = 0.54 nm	d < 25 nm	$30 \times 100\ nm^2$	d = 44 nm	100 nm
μ (D)	8	29	60	92	20
$\gamma_0/2\pi$ (meV)	2×10^{-5}	4×10^{-4}	0.003	0.015	30
$\gamma/2\pi$ (meV)	2×10^{-5}	0.09	0.08	0.28	
Coupling					
$2g/2\pi$ (meV)	3×10^{-4}	0.17	0.16	0.81	50-150

Figure 4.10 Comparison of optical resonators and plasmonic nanotriangle. (reproduced from [60]).

4.8 Anticrossing

A strongly interacting system can be characterized by anti-crossing behaviour. A system that consists of two coupled oscillators can be identified by two natural frequencies. When the coupling between the oscillators strengthens, the energy separation (energy splitting) between these two oscillators increases. This can be considered as repulsion between the frequencies, as the lower frequency decreases and the higher increases. Anticrossing in energy with a separation is known as vacuum-Rabi splitting. An example of anti-crossing behaviour for a core-shell nanoparticle is illustrated in Figure 4.10 [120]. Here, the core is silver and the shell is a resonant molecule. Scattering and absorption spectra are calculated by keeping the core radius and the plasmon resonance constant and by varying the molecular resonance relative to the plasmon resonance. The spectra are plotted for the three different coupling regimes: enhanced absorption (Figure 4.10a), induced transparency (Figure 4.10b) and strong coupling (Figure 4.10c). For enhanced absorption and induced transparency cases, the scattering plots show a small peak splitting. However, the absorption plots do not show anticrossing behaviour. In the strong coupling case, the anticrossing behaviour is clear in both scattering and absorption spectra.
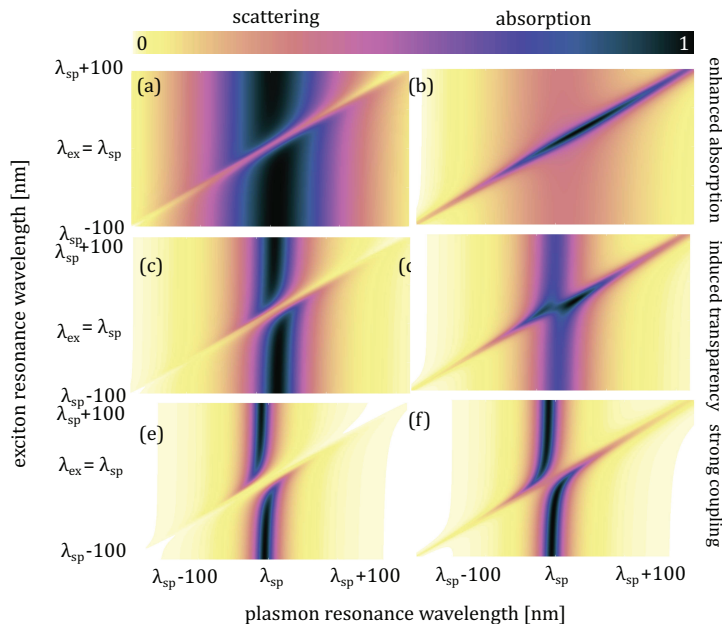
Figure 4.11. Appearance of anticrossing behaviour between plasmonic and molecular resonances from enhanced absorption to strong coupling. The left column is scattering and the right column represents the absorption spectra.

Chapter 5

Experimental Methodology

In this chapter, general background about the material, sample preparation, and characterization methods used in attached papers are presented. In Paper 1 and Paper 3, silver colloidal (BBI Solutions and Sigma-Aldrich) particles stabilized by citrate were used. In Paper 2, silver nanotriangles are synthesized by photoinduced conversion method [121]. In Paper 3 Ag particles are coated with thiolated Rhodamine 6G and Paper 1 and 2 is about colloidal Ag nanorods coated with J-aggregates. The details of how to coat Ag particles by the dyes are given in the attached papers, along with the details about the equipment and parameters used.

5.1 Self-assembled monolayers (SAM)

There are different ways of immobilizing fluorescent emitters on metal surfaces, such as by, physical and chemical interactions. One of the most common immobilization methods is the adsorption of molecules on metal surfaces via organic thiol chemistry. Thiols have strong affinity towards noble metal surfaces. With thiol chemistry, it is possible to engineer organic surfaces on metal surfaces with various chemical functionalities [122]. For example, thiols such as alkanethiols can adsorb on gold (Au), silver (Ag), and copper (Cu) and form self-assembled monolayers. The adsorption of thiols on these metals show structural differences due to the differences in reactivity of the surface of the metal (i.e. especially oxidation of the surface) [123].

5.2 Tween 20

Polyoxyethylene (20) sorbitan monolaurate, also called Tween 20, is a nonionic surfactant used to prevent irreversible aggregation upon chemisorption of alkanethiols on colloidal metal nanoparticles. In Paper 3, colloidal Ag nanoparticles were coated with thiolated Rhodamine 6G in the presence of Tween 20. The physical adsorption of Tween 20 onto metal nanoparticles prior to adsorption of thiol stabilizes the particles against aggregation by the oligo(ethylene glycol) subgroup of Tween 20 [124]. The interaction between metal (Au/Ag) surfaces and Tween 20 is weaker than the interaction between metal surfaces with alkanethiols (i.e. physisorption versus chemisorption). The weakly adsorbed surfactant could be subsequently displaced by alkanethiols chemisorbing onto the metal surface. Fusion of the metallic cores of particles is one of the mechanisms causing irreversible aggregation of colloidal particles. Tween 20 prevents aggregation by acting as an

intermediate layer preventing the fusion of the particles until colloids are completely covered by a monolayer of thiols. Figure 3.4 illustrates the mechanism of Tween 20, namely the prevention of the aggregation of colloidal particles upon binding of thiol to colloidal particles [124].
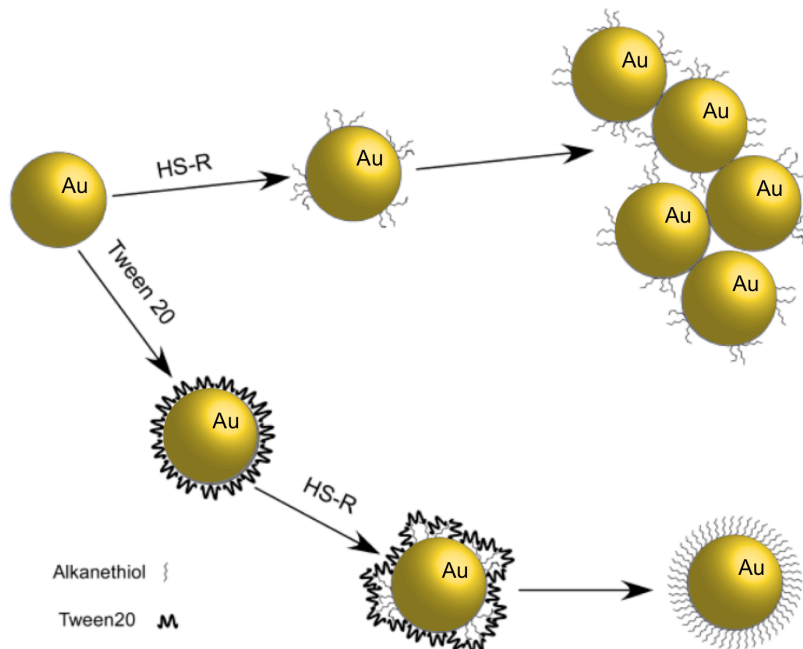
Figure 5.1 - Scheme showing the formation of thiols on colloidal Au particle by using tween 20 (adapted from [124]).

5.3 Immobilization of colloidal nanoparticles on cover glass

Poly-L-lysine, APTES ((3-Aminopropyl)triethoxysilane) and APTMS ((3-aminopropyl)-trimethoxysilane) are used in our papers to attach silver or gold colloidal particles to glass substrates.

Poly-L-lysine is a positively charged polymer of the essential amino acid L-lysine. There is approximately one HBr per lysinein its structure as seen in Figure 3.5. HBr makes poly-L-lysine become in a crystalline form soluble in water. Poly-L-lysine has been widely used for cell adhesion on different substrates such as cover glass. Similarly we used poly-L-lysine to enhance silver and gold colloidal nanoparticle attachment on cover glass. Since poly-L-lysine is positively charged, it increases the positively charged sites available for particle binding and therefore, the electrostatic interaction between negatively charged particles. This also prevents aggregation of particles on the surface. The particles prepared with this method become well separated and suitable for single particle measurement.
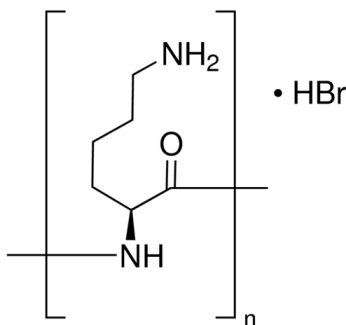
Figure 5.2 – Chemical structure of polylysine molecule (Source: Sigma Aldrich)

Poly-L-lysine is first solved in water with 0.25 mg/ml to 1 mg/ml concentration. Then poly-L-lysine is drop casted on a clean cover glass. After 5 minutes of incubation, the cover glass surface is rinsed with water. Particles are then drop casted on the cover glass surface. The incubation time of the particles on cover glass depends on the concentration of the particles to be achieved, and this varies been 2 and 5 minutes in the experiments.

The particles adsorbed to cover glass with poly-L-lysine stay quite stable on the surface. However if the electrostatic interaction is changed for example by addition of buffer solutions, then the particles can be removed from the surface. In that case using APTES or APTMS can give more stable particle immobilization.

Both **APTES** and **APTMS** functionalize glass surface through self-assembly of alkoxysilane molecules, which is called the silanization process. APTES has ethoxy (-OCH$_2$CH$_3$) and APTMS has methoxy (-OCH$_3$) groups [125] as shown in Figure 3.6. These alkoxy groups react with hydroxyl groups on glass or metal oxide surfaces resulting in formation of covalent Si-O-Si bonds. NH$_2$ groups make bonds with silver and gold nanoparticles [126,127].
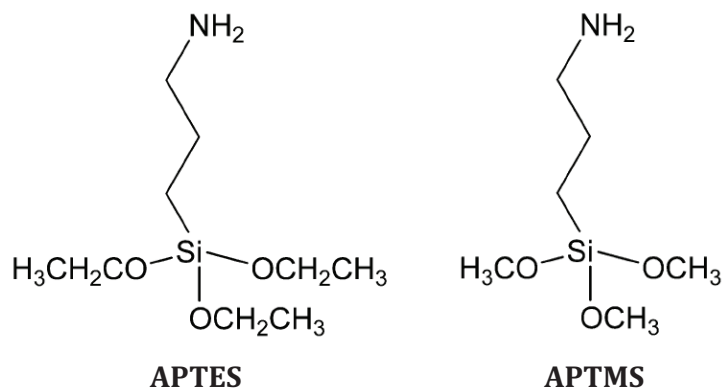
Figure 5.3 – Chemical structure of APTES and APTMS (reproduced from [125]).

To immobilize the silver or gold colloidal nanoparticles we used the following recipe. First a 10% volume APTES in ethanol or 10% volume APTMS in methanol is prepared. Then a clean cover class is dipped into the solution and left for minimum 5 minutes. It is then rinsed with ethanol or methanol. After drying with a nitrogen gun, silver or gold colloidal particles are drop casted. Particles are incubated depending on the concentration achieved.

5.4 Quantum dot attachment on gold nanoparticles

For the directionality project, the aim was to attach quantum dots on gold surfaces using the following recipe, which is adapted from the following report [128].

Streptavidin conjugated CdSe/ZnS quantum dots were attached to the gold surface by means of thiol chemistry. Gold nanoparticles fabricated by hole-mask colloidal lithography were first functionalized with biotin through thiol bonds.

First, 7% wt biotin-CONH-PEG-CO-C_2H_4-SH, 5 kDa, purchased from Rapp Polymere (SH-PEG(5)-biotin) and 93% wt HO-PEG-NHCO-C_2H_4-SH, 3 kDa, purchased from Rapp Polymere (SH-PEG(3)), were mixed in order to optimize the concentration of biotin on gold surface. The final concentration of the mix becomes 0.3 mg/ml in HEPES buffer solution (0.01 M, add 0.9M K_2SO_4, pH 7.4). The nanoparticles substrates were incubated in the mix for 60 minutes. Excess material was rinsed from the surface with milli-Q water by letting substrates to stay in milli-Q water for 30-60 minutes. Then the substrates were dried with a nitrogen gun. This step functionalizes the gold part of the substrates with biotin.

As a second step, the glass part of the substrates was protected from non-specific binding of quantum dots by using poly-L-lysine modified polyethylene glycol, PLL(20)-g(3.5)-PEG(2), purchased from Susos (PLL-g-PEG). PLL-g_PEG attaches to the glass surface through electrostatic interaction. PLL-g-PEG was prepared in 0.01 mg/ml concentration in a HEPES buffer (0.01M, add 0.15M NaCl, pH 7.4). The substrates were incubated in the solution for 30-60 minutes, rinsed in milli-Q water for 30-60 minutes, and then dried with a nitrogen gun.

Finally, streptavidin conjugated quantum dots were drop casted on the substrates. Streptavidin conjugated quantum dots were purchased from Life Technologies. 1 μM stock solution of quantum dots was diluted 200 times for the final concentration of 5 nM in the TRIS buffer (0.1M, add 0.15M NaCl, pH 8.2). The solution was drop casted on substrates and left for stay for 30-60 minutes. The substrates were rinsed in milli-Q water for 30-60 minutes and finally dried with a nitrogen gun.

This method provides uniform and reproducible quantum dot attachment on gold nanoparticles. The binding kinetics of each step was monitored with refractive index dependent plasmon resonance as shown in Figure 4.1. The fluorescence image of the

resultant quantum dot immobilized gold nanoparticles is shown in Figure 2.7. Note that the fluorescence image of the laser illumination is not completely uniform. We observed that the thiol chemistry described above does not work when the nanoparticles contain both gold and silver, such as, like bimetallic vertical nanoantennas most probably due to the Oswald ripening effect mentioned in Chapter 2, directional emission section.

5.5 Hole-mask colloidal lithography

Hole-mask colloidal lithography (HCL) technique [14] was used to fabricate nanodisks on a glass surface for Paper 3, Paper 4 and bimetallic vertical and horizontal nanoantennas as a continuation work of Paper 4. The fabrication steps are illustrated in Figure 5.4.

First a sacrificial resist layer is deposited on substrate by spin coating. Poly(methyl methacrylate) (PMMA) is one of the common resist used in hole-mask colloidal lithography (step 1). Spin rate is determined according to the aimed thickness of the resist and nanoparticles thickness and shape. The substrate is then baked in an oven to make the resist hard. In order to make the surface of hydrophilic, the substrate is exposed to mild oxygen plasma. Then PDDA, which is a negatively charged polymer, and the positively charged polystyrene beads are dropped, rinsed, and dried from PMMA surface (step 2). 10 nm sacrificial gold is evaporated on top of the sample (step 2). Polystyrene beads are tape-stripped (step 3). Then PMMA is exposed to oxygen plasma for etching till of the substrate to make holes (step 4). The desired height of the material is evaporated with the desired angle (step 5). PMMA is removed by dissolving in acetone (step 6).

Step 6 in Figure 5.4 shows the resulting structures used in the papers. Silver nanodisks are used in Rhodamine 6G work in Paper 3. Polystyrene beads with 80 nm diameter were used. 25-32 nm silver was evaporated on top of a 2 nm chromium layer for the purpose of adhesion. Silver-gold vertical nanoantennas are used as in the directionality study, which is continuation of Paper 4. 150 nm polystyrene beads were used in this study. 40 nm silver, 30-40-50 nm aluminum oxide, and 30 nm gold were sequentially evaporated. In the antenna structure, the bottom disk is silver with a 150 nm diameter and 40 nm height. The top disk is gold with a ~80-100 nm diameter (depending on spacer thickness) and 30 nm height. The two disks are separated with an aluminum oxide spacer of different thicknesses. Finally, silver vertical nanoatennas are used in Paper 4. SEM images of the samples were shown in Figure 5.7

step 1: deposition of sacrificial resist later and polystyrene beads

O O O   polystyrene beads
           pmma
           substrate

step 2: evaporation of 10 nm gold mask

↓ ↓ ↓ ↓   ↘ ↘ ↘ ↘

O O O   O O O
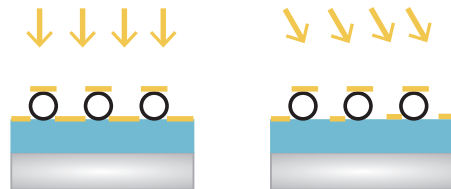
step 3: tape-stripping of polystyrene beads

O O O
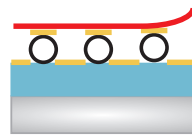
step 4: oxygen plasma etch

↓ ↓ ↓ ↓
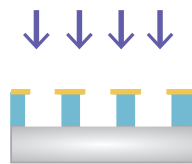
step 5: material evaporation: silver and gold

↓ ↓ ↓ ↓ Ag

↓ ↓ ↓ ↓ Au
↓ ↓ ↓ ↓ Al_2O_3
↓ ↓ ↓ ↓ Ag

Ag   Au
↘ ↘   ↙ ↙

step 6: lift-off

Ag nanodisks

Ag-Au vertical
nanoantenna
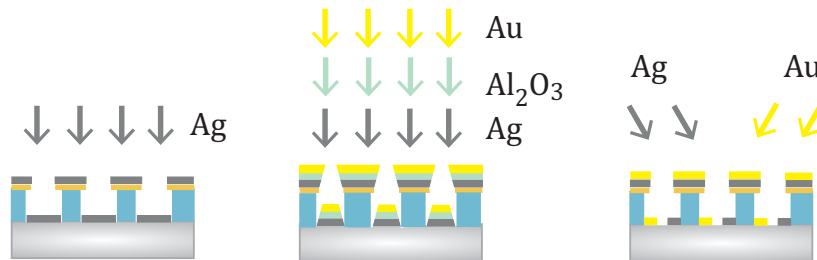
Ag-Au horizontal
nanoantenna
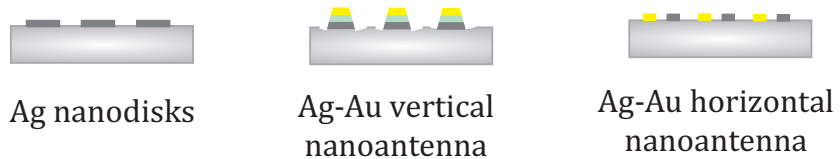
Figure 5.4 – The fabrication steps of sample preparation for Ag nanodisks, bimetallic vertical and horizontal nanoantennas.
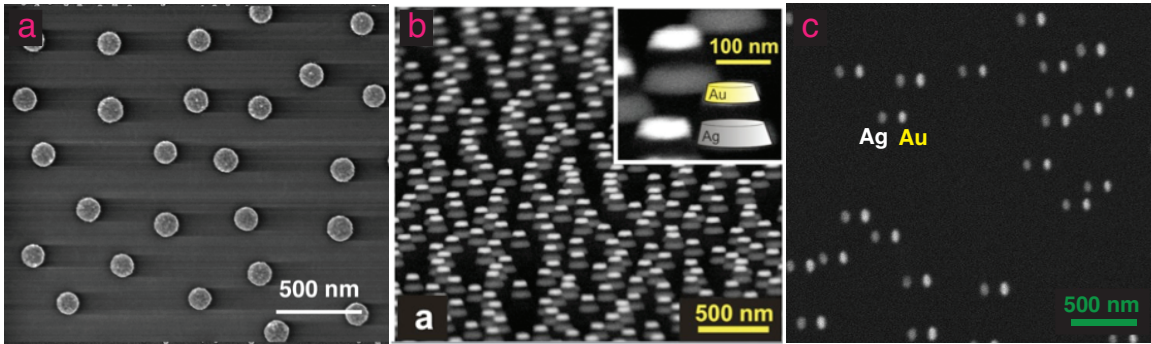
Figure 5.5 – SEM images of nanoparticles fabricated by hole-mask colloidal lithography. (a) silver nanodisks. (Thanks to Alexander Dmitriev) (b) Ag-Au bimetallic vertical nanoantennas. (c) Ag-Au bimetallic horizontal nanoantennas.

5.6 Dark-field microscopy

Dark field microscopy is a widely used microscopy technique to image unstained samples. This technique is based on blocking the central light along the optical axis that passes through the specimen without scattering. In terms of Fourier optics, 0th order diffraction is removed, such that only oblique rays emerging from scattering of the specimen are collected. This produces an image of bright objects with a dark background, which is constructed from higher order diffraction. The central light is blocked using a specific disk size and remaining light is focused on the sample via a condenser lens. The condenser lens has a higher numerical aperture than the objective, such that the sample is illuminated with a high angle of incidence and only scattered light is collected. While transmission configuration requires transparent samples, non-transparent samples are measured in reflection mode. Figure 5.6 illustrates the schematic of dark-field microscopy in transmission mode. Figure 5.7 shows colloidal Ag nanoparticles on a cover glass, as imaged by dark-field microscopy. In the image, Ag particles have different colours owing to the fact that they scatter light at different wavelengths due to their plasmon resonance wavelength, which varies with geometry (e.g. size and shape).
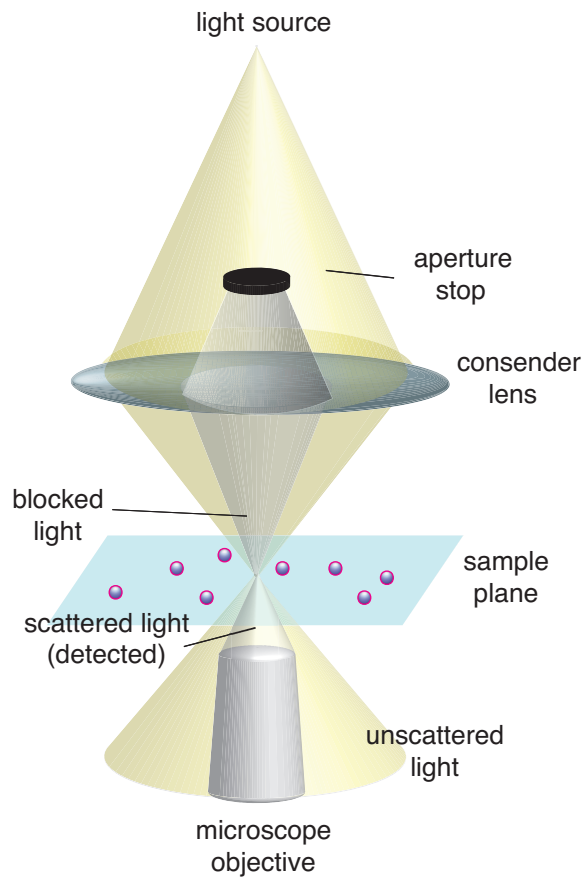
Figure 5.6 - Schematic diagrams showing light path of dark field microscope in transmission mode
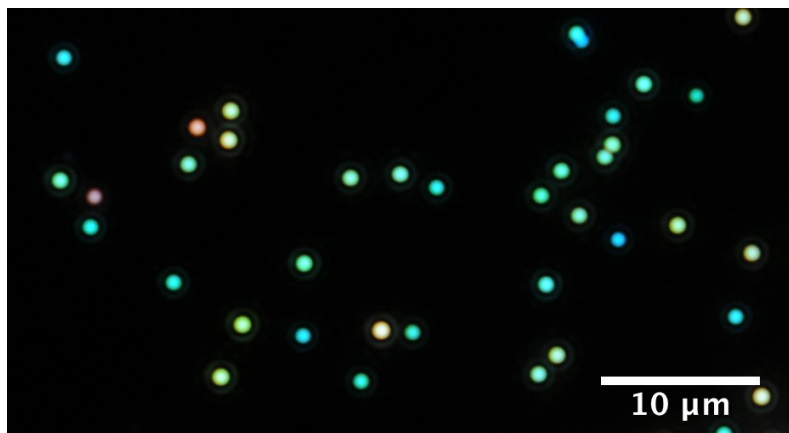
Figure 5.7 - Dark field microscopy image of colloidal silver nanoparticles on a glass cover slide.

5.7 Fourier Imaging

Fourier imaging means imaging the back focal plane of the objective lens. It is important because it provides information that cannot be collected with ordinary dark field imaging technique. For instance by means of this technique it is possible to image the emission pattern of single molecule to determine its orientation [129] or the emission pattern of a nanoantenna as described in the attached Paper 4.

Figure 5.8 shows the calculated emission pattern of a dipole at the air-glass interface at the back focal plane of the objective. Figure 5.8-b and c are the emission patterns of horizontal dipoles, Figure 5.8-d is a vertical dipole and Figure 5.8-e is for the dipole standing in the diagonal.
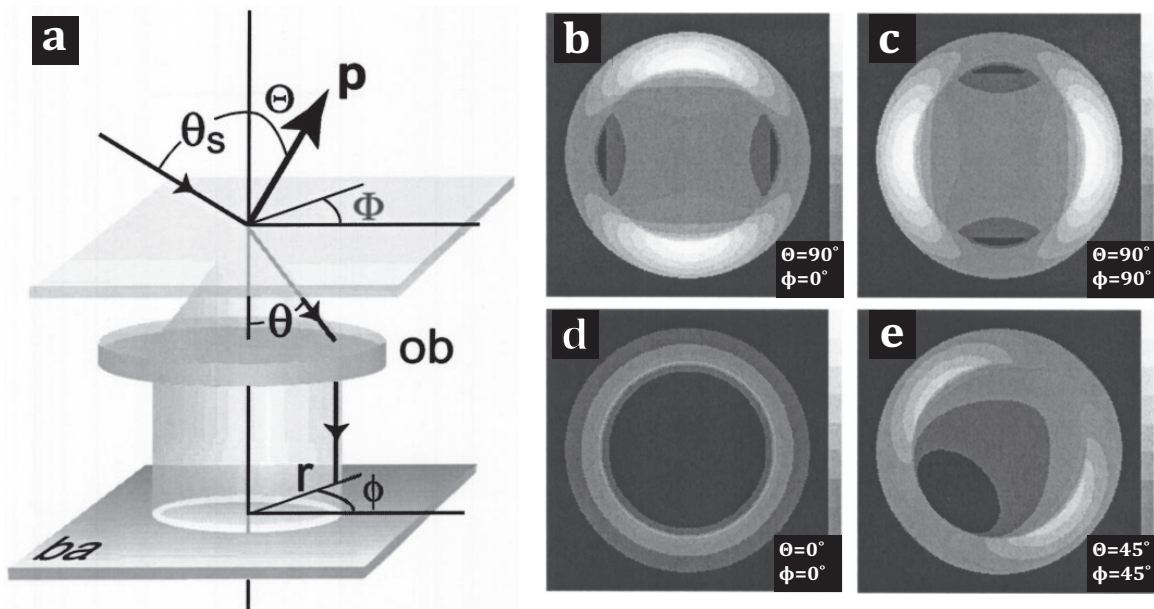
Figure 5.8 – (a) schematic illustration of a dipole with dipole moment p, sitting at the air-glass interface. Ob stands for objective lens, ba stands for back aperture of the objective. (b,c,d,e) for emission patterns of a dipole sitting on air–glass interface calculated at the back focal plane of the objective with different orientations. (Reproduced from [129])

The emission pattern was collected by collecting the emitted photons with an objective lens and by imaging the intensity distribution in the objective's back focal.

Fourier imaging can be done by means of a 4f correlator scheme. Positioning an opaque mask can work as a low pass filter and block the incident light.

The incident radiation was blocked from reaching the detector by an opaque stop

installed in the secondary Fourier plane. The diameter of the opaque stop corresponded to NA < 0.9, so that the light emitted at higher angles could pass through.

5.8 Fluorescence microscopy

Fluorescence microscopy is another common imaging technique which uses fluorescence and phosphorescence emission as a contrast signal compared to background. Fluorescence microscopy is based on illuminating fluorophores and collecting the emission light, which has higher wavelength than the illumination wavelength. For this purpose, excitation filters, emission filters, and dichroic mirrors are used which are chosen according to the excitation and emission spectrum of the fluorophore. Figure 5.9 shows the basic fluorescence microscopy configuration. The emission filter only allows certain wavelengths to enter to the filter cube. A dichroic mirror then reflects incoming light and directs it towards the objective. Fluorescence emission from the dye is collected by the objective. Objectives with higher numerical apertures are preferred in order to collect more light. The light then passes through the dichroic mirror and then the emission filter. The Figure 5.10 shows a fluorescence microscopy image of Ag colloidal nanoparticles coated by thiolated Rhodamine 6G. Because the size and the shape of the particles are different, varying intensity and colour of Rhodamine 6G can be observed. The variation is due to the modification of fluorescence by plasmonic nanoparticles.
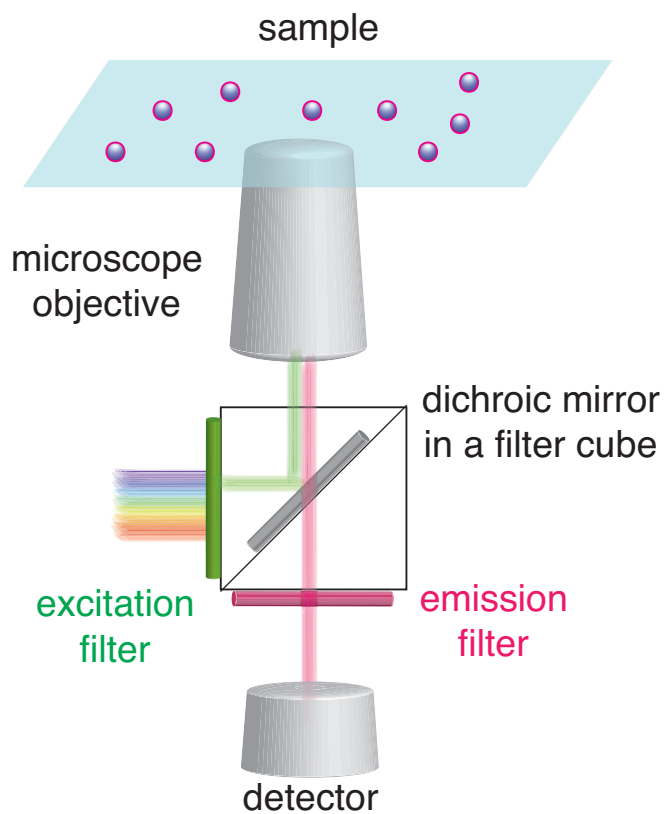
Figure 5.9 Schematic diagrams showing light path of fluorescence microscope
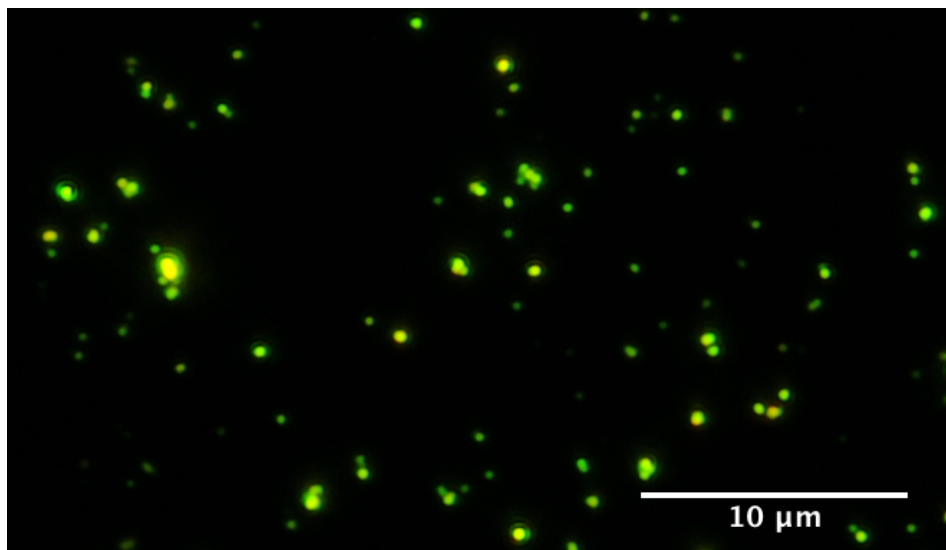
Figure 5.10 Fluorescence microscopy image of colloidal Ag nanoparticles coated by thiolated Rhodamine 6G

5.9 Hyper spectral imaging with liquid crystal tunable filter

Hyperspectral imaging is an imaging technique, based on collecting the spectrum for each pixel in an image and extracting the spectrum of a chosen pixel. The concept of hyper spectral imaging is illustrated in Figure 5.11.
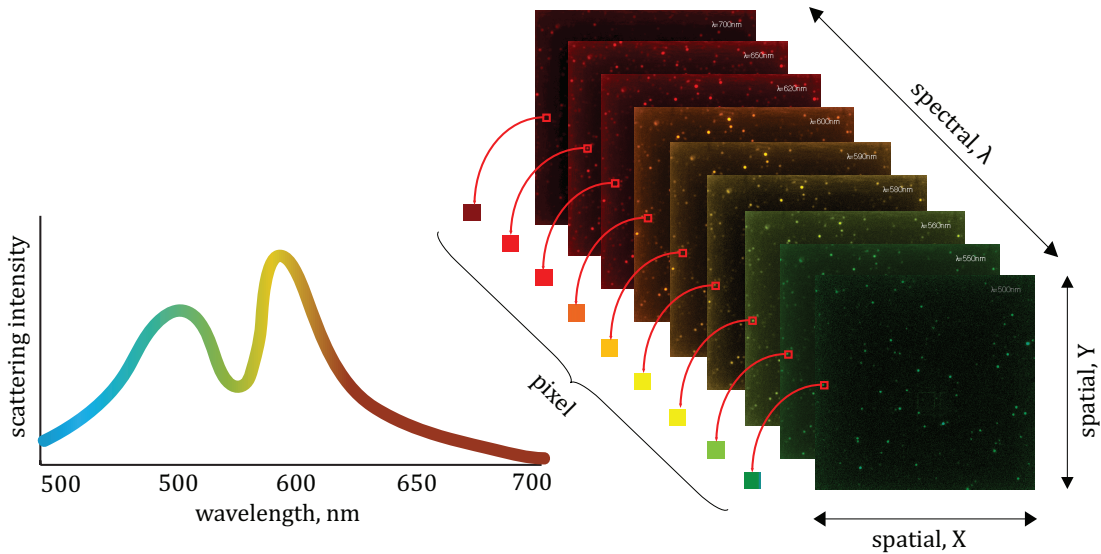
Figure 5.11 – Illustration of hyper spectral imaging.

Liquid crystal tuneable filters are used for hyper spectral imaging purpose. They are based on the optical filter design described by Bernard Lyot in 1933, which provides only a static bandpass. A Lyot cell consists of two linear polarizers, a fixed retarder and liquid crystal cell. Liquid crystals variable retarders are added to the Lyot's design to provide spectral tuning ability. Typically liquid crystal tunable filters consist of min 12 stages. Figure 5.12 shows the basic stage of a Lyot cell.
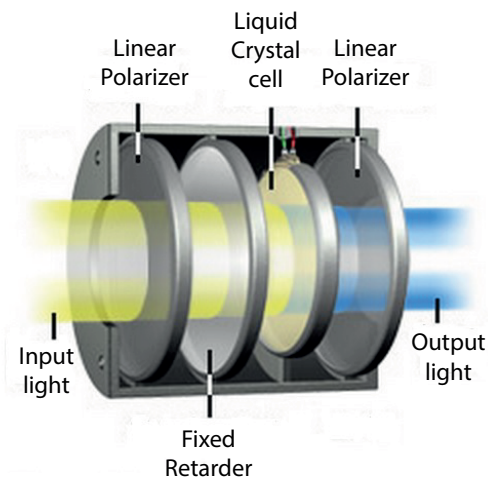
Figure 5.12- Structure of Lyot cell (reproduced from http://www.microscopyu.com)

Each tunable stage transmits light with sinusoidal intensity as a function of wavelength. The product of transmitted light from each stage gives a narrow range of wavelengths by constructive interference in the desired bandwidth range and destructive interference in the other range. The transmission of the light outside of the passband range is usually 0.01% or less. Figure 3.15 shows the transmission after 6 stages [130].
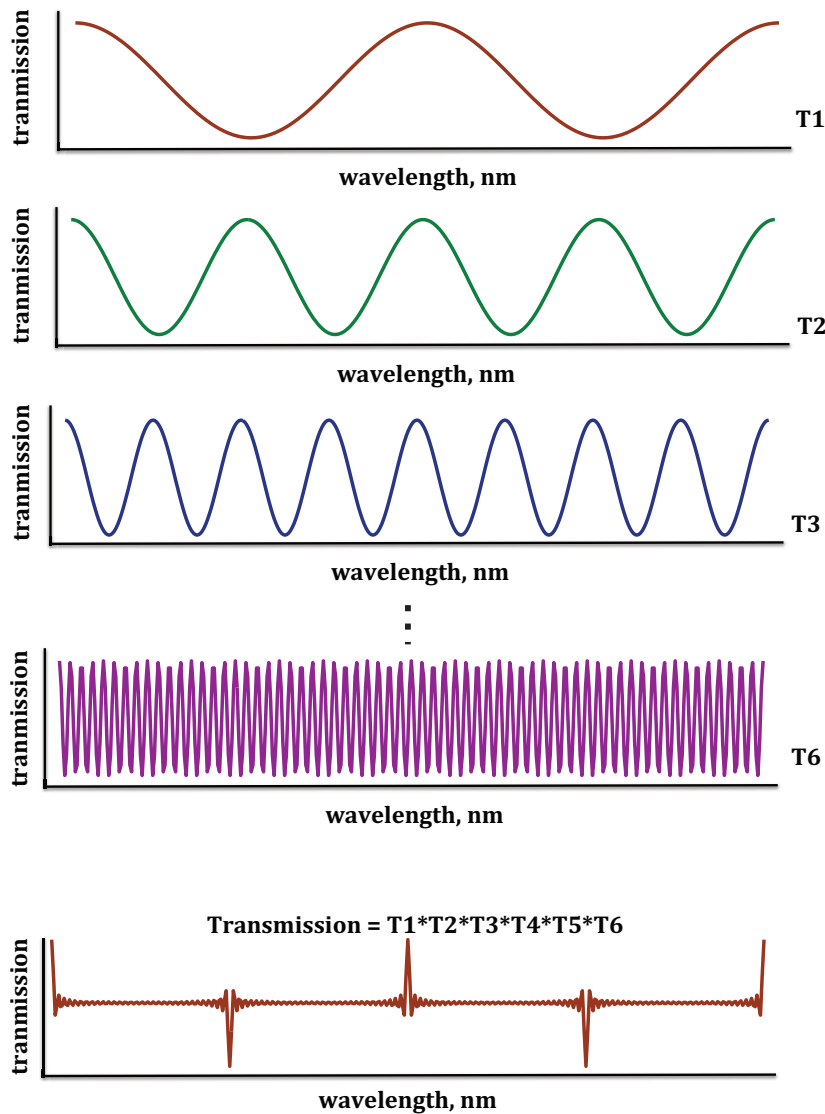
Figure 3.15 – Transmission profile through six stages of a Lyot cell [130]

Chapter 6

Summary and Outlook

Paper 1. *Approaching the strong coupling limit in single plasmonic nanoparticles interacting with J-aggregates* is a study of single silver nanorod interacting with sheets of J-aggregate cyanine dye. We observed very strong dips in scattering spectra which we attribute to strong interaction between localized surface plasmons of silver nanoparticles and electronic excitations in the molecular J-aggregate. The scattering spectra show about 50% transparency, which are the largest dips reported to our knowledge at the single particle level. The reason why J-aggregates showed stronger dips in scattering is the high oscillator strength of the molecule, the narrow molecular resonance width, and small silver particle volumes. We studied this coupled molecule-plasmon system with a classical model, where two harmonic oscillators are coupled to each other. We fitted the model to scattering spectra of 20 different individual silver nanorods coupled to molecular J-aggregates. The parameters obtained from the model showed an anti-crossing behavior, which is attributed to a strong coupling regime. Moreover, we analyzed the system by using an analytical model. A core-shell model was used to calculate polarizability of the dye-particle structure. We found that the transparency dips in scattering spectra increase with higher surface to volume ratios of the particles. In other words, smaller particles show less radiative damping and narrower plasmon width, and have more dye molecules per metal atom in the core. This results in a stronger interaction between dye molecules and plasmonic particles.

Paper 2. *Realizing strong light-matter interactions between single nanoparticle plasmons and molecular excitons at ambient conditions.* This paper is a follow-up continuation of Paper 1. In this paper we studied interaction of molecular J-aggregates with silver nanotriangles at the single particle level. Silver nanoparticles have large size distribution and it is possible to obtain very small volumes in the same batch. We obtained different interaction regimes such as strong coupling, electromagnetically induced transparency, weak coupling, Fano shape and even 3-peaked spectra at single particle level. We mainly attributed the variation in spectra to varying mode volumes of the particles and varying spectral overlap between the plasmons and the molecular resonances. In contrast to Paper 1, we used a liquid crystal tunable filter for spectroscopic measurements, which allows high throughput hyper-spectral imaging of many individual particles simultaneously.

Another important contribution in this paper is imaging J-aggregates interacting with silver particles with SEM, TEM and AFM techniques. There are very few studies about formation and structure of J-aggregates of the TDBC molecules. We tracked the formation of J-aggregates and imaged how they attach to silver nanoprisms. The

results indicates that the J-aggregates are layered sheet-like structures and that the silver nanoprisms lie on top of the sheets when they are adsorbed on a substrate.

Paper 3. *Interactions between nanoparticle plasmons and Rhodamine-6G: strong coupling or enhanced absorption?* is a report about observing dips in the scattering spectra of R6G coated silver particles at the ensemble and the single particle level. For the ensemble measurements, the silver particles were fabricated by hole-mask colloidal lithography. Scattering measurements were made at ensemble level. These spectral dips correspond to the wavelengths where R6G has absorption features. We used a new form of R6G which has a thiol end group. The thiol group makes it possible to adsorb R6G on silver specifically and densely. This is an important effect because the number of molecules interacting with plasmonic nanoparticles affects plasmon-molecule interaction. Another effect that influences the number of molecules adsorbed on the plasmonic nanoparticles surface is the solubility of dye molecules. Both ordinary R6G and thiolated R6G have lower solubility in water. Scattering spectra of R6G adsorbed silver nanoparticles were compared for two different dyes (thiolated vs. ordinary R6G) in two different solvents (water vs. methanol). The number of molecules absorbed on the surface was quantified by thiol exchange experiments. The estimated number of molecules shows agreement with previously reported values. Thiolated R6G in methanol showed similar number of molecules like self-assembled monolayers, while ordinary R6G resulted in sub-monolayer coverage. Both dyes had more molecules adsorbed on the silver surface due to lower solubility in water. Thiolated R6G had structures similar to micelles formed because of its hydrophobic thiol and hydrophilic dye parts. Scattering experiments were also performed for individual colloidal silver nanoparticles coated with R6G. These spectra showed spectral dips as well. FDTD simulations were performed for ensemble measurements and Mie theory calculations were done for single particle measurements to understand the mechanism behind the spectral dips. They both showed good agreement with the experimental scattering spectra and the estimated number of molecules. The calculated absorption spectra suggested that surface enhanced absorption is the main mechanism behind the spectral changes in this case. This is an important result because in previous studies similar spectral dips were attributed only to strong coupling between the molecule and plasmonic nanoparticles.

Paper 4. A *bimetallic nanoantenna for directional color routing* is about experimental realization of bimetallic nanoantenna dimers that scatter red and blue light in opposite directions. These bimetallic nanoantennas consist of closely spaced silver and gold nanodisks made by hole-mask colloidal lithography as compact as $\sim\lambda^3/100$, where λ is the wavelength of visible light. Scattering from the dimer nanoantennas was collected at the back focal plane of the microscope system, so called Fourier plane, by blocking the transmitted incident light with an opaque stop with a corresponding size of the critical angle. Dimers show directional emission when they are illuminated with both perpendicular and parallel-polarized incident light to the dimer axis. Simulations reveals that the mechanism behind this color routing property comes from maximizing interference in one direction, which was

achieved by using two different material composition. Indeed, there is a difference in permittivities of gold and silver nanodisks. Gold nanodisk supports interband transitions between a wavelength region of 400-500 nm, which increases the imaginary part of its permittivity. On the other hand, silver nanodisks do not have interband transitions within this wavelength region. This difference results in a positive phase shift in the blue part of the spectrum, thus scattering of different wavelengths in different directions. Furthermore this concept is explained by an analytical simulation of two weakly interacting induced dipoles in metal particles, where the relative phase shift between two resonances in monometallic and bimetallic dimers are compared.

Several directions can be taken to proceed in this field as continuation work:

Absorption measurements at the single particle level rather than scattering measurement would be a more direct way to understand the main mechanism behind plasmon-molecule interactions. Single particle scattering measurements in smaller particles becomes challenging due to lower radiative damping rates of plasmonic nanostructures. This puts even more emphasis on the need of measurements in absorption rather than scattering, since absorption becomes the dominant effect when particles become smaller. On the other hand, single particle absorption measurements are experimentally difficult to achieve. Developing a method which enables single particle absorption measurements would be an important step.

A very interesting and rare three-peaked spectrum was obtained for nanotriangle-J-aggregate coupled system. Even though the coupled harmonic oscillator model suggests that interaction between two different J-aggregates with slightly different linewidths and a single silver nanoprims could be the mechanism behind this, FDTD simulations did not predict the three-peaked observations. Further study should be performed to understand the physics behind this effect.

Single nanotriangles are the main focus in the J-aggregate papers. As a continuation investigation of dimers, trimers and more complicated structures can be done. These structures have stronger hot spots which might result in stronger or more complicated coupling.

Additional work can be done on molecular J-aggregates in different perspectives. Further understanding structure, formation and binding of J-aggregate molecules on metal nanostructures will open up more room for molecular plasmonics. Stability of J-aggregates is another direction to go. It has been shown that they can easily break up into monomers by laser illumination. Embedding J-aggregates into metal oxide layer could be an option to stabilize the dye.

Thiolated R6G has potential to provide an advantage over ordinary Rhodamine 6G in various applications which involve specific and selective binding of the molecule to nobel metal surface. Thus by designing SERS substrates with different materials,

it can be possible to densely attach R6G to specific positions on the substrate. For instance, immobilizing R6G specifically on hotspots can enable stronger SERS enhancement factors.

Thiolated R6G has a strong advantage over ordinary R6G in terms of having densely packaged molecules on silver particles. However, Paper 3 indicated that the effective oscillator strength became lower when they were too closely packed. The mechanism behind should be further investigated. Mixing smaller thiols, such as 6-mercapto-1-hexanol, with thiolated R6G may optimize spacing between R6G molecules. Moreover, the structural configuration of thiolated R6G on silver nanoparticles is not known. Orientation R6G molecule with respect to dipole orientation in plasmonic nanostructure affects coupling between the molecule and the nanostructure. Density functional theory can be used to understand configuration of thiolated R6G on silver surface. More comparative studies between ordinary and thiolated R6G can be done for deeper understanding, such as monitoring binding kinetics with localized surface plasmon resonance sensing or quartz crystal microbalance.

Another possible future work could be studying the molecule-plasmon interaction at low temperatures. Even though thiolated R6G increases the number of molecules attached to silver nanoparticles, the interaction is basically surface-enhanced absorption. The linewidth of Rhodamine 6G can be decreased in low temperatures by eliminating homogeneous broadening. Having a smaller linewidth can help to attain stronger molecule-plasmon interaction.

Finally, for directional emission from bimetallic nanoantennas, the next natural step is attaching an emitter to the nanoantenna and realizing the directional emission from the emitter. Actually this was what we continued with in vertical nanoantennas by using streptavidin-biotin chemistry to attach quantum dots. However, we think that the surface chemistry probably failed to work due to the Oswald ripening effect in the presence of silver nanoparticles. Different surface chemistry techniques and different configurations remain to be tested further.

Acknowledgements

This thesis became possible with the contribution and support of many people. I would like give thanks to

First of all, my supervisor **Mikael Käll** I am grateful for giving me the opportunity to work in this group. Thank you for providing this nurturing and free research environment. It helped me to develop myself a lot both scientifically and personally. Thank you for your guidance.

My co-supervisor **Timur Shegai** thank you for your enthusiasm, all your support and guidance during this journey. I learned a lot from you as my scientific mentor, both in the lab and from our discussions about science.

Tomasz Antosiewicz thank you for all your valuable theoretical contribution and helpful discussions, which gave an important understanding to my work.

Martin Wersäll thank you for nice collaboration for J-aggregate paper and your valuable contribution.

Tina and **Kasper** thank you for your nice collaboration in Rhodamine 6G paper.

Tomasz, Viktoria, Inès, Simone, Mike, and **Laura** thank you for taking your time and proofreading parts of this thesis.

Si, Ruggero, Lei, Yurui, **Micke, Virginia, Robin, Vladimir**, **Kristofer** and **Kristof** thank you sharing lab experience with me, for your help in the lab practicalities and sample preparation.

Gustav, Andreas, Anni, **Virginia** and **Mitra**, thank you sharing the office with me, and for our scientific, and non-scientific conversations, and our nice times.

The whole **Bionanohotonics** group for nice moments all together. To the all group members, for fun times in beers tastings, fikas, lunches, dinners, and trips.

All the colleagues from **Biological Physics, Chemical Physics**, **Physical Chemistry**, and **MC2** for creating a nice working environment. **Viktoria**, **Deborah**, **Mokhtar, Anna**, **Fernando, Mike, Adriana, Sandra, Simone, İrep, Aldo, Alar** and **Rafael** for all nice times together and your friendship.

Malin Bäckström, Elisabeth Thomsson, and **Richard Lymer** thank you for helping with cell cultivation and our discussions. **Julia Fernandez-Rodriguez** and **Maria Smedh** for help with live cell imaging and fruitful discussion.

References

[1] X. Fan, W. Zheng, D.J. Singh, Light scattering and surface plasmons on small spherical particles, Light Sci. Appl. 3 (2014) e179.

[2] F. Della Sala, S. D'Agostino, Handbook of molecular plasmonics, Pan Stanford, Singapore, 2013.

[3] W.L. Barnes, A. Dereux, T.W. Ebbesen, Subwavelength optics, Nature. 424 (2003) 824–830.

[4] A. V Zayats, I.I. Smolyaninov, A.A. Maradudin, Nano-optics of surface plasmon polaritons, Phys. Rep. 408 (2005) 131–314.

[5] J.A. Schuller, E.S. Barnard, W. Cai, Y.C. Jun, J.S. White, M.L. Brongersma, Plasmonics for extreme light concentration and manipulation, Nat. Mater. 9 (2010) 193–204.

[6] E. Ozbay, Plasmonics: merging photonics and electronics at nanoscale dimensions, Science. 311 (2006) 189–93.

[7] N.J. Halas, Plasmonics: an emerging field fostered by Nano Letters, Nano Lett. 10 (2010) 3816–22.

[8] J. Zhao, L.J. Sherry, G.C. Schatz, R.P. Van Duyne, Molecular plasmonics: chromophore–plasmon coupling and single-particle nanosensors, IEEE J. Sel. Top. Quantum Electron. 14 (2008) 1418–1429.

[9] M.S. Tame, K.R. McEnery, Ş.K. Özdemir, J. Lee, S. a. Maier, M.S. Kim, Quantum plasmonics, Nat. Phys. 9 (2013) 329–340.

[10] T. Shegai, V.D. Miljkovic, K. Bao, H. Xu, P. Nordlander, P. Johansson, et al., Unidirectional broadband light emission from supported, Nano Lett. 11 (2011) 706–711.

[11] A.G. Curto, G. Volpe, T.H. Taminiau, M.P. Kreuzer, R. Quidant, N.F. van Hulst, Unidirectional emission of a quantum dot coupled to a nanoantenna., Science. 329 (2010) 930–3.

[12] T.H. Taminiau, F.D. Stefani, N.F. van Hulst, Single emitters coupled to plasmonic nano-antennas: angular emission and collection efficiency, New J. Phys. 10 (2008) 105005.

[13] Y.B. Zheng, B. Kiraly, P.S. Weiss, T.J. Huang, Molecular plasmonics for biology and nanomedicine., Nanomedicine (Lond). 7 (2012) 751–70.

[14] H. Fredriksson, Y. Alaverdyan, A. Dmitriev, C. Langhammer, D.S. Sutherland, M. Zäch, et al., Hole–mask colloidal l ithography, Adv. Mater. 19 (2007) 4297–4302.

[15] J. Homola, S.S. Yee, G. Gauglitz, Surface plasmon resonance sensors: review, Sensors Actuators B Chem. 54 (1999) 3–15.

[16] S. Nie, S. Emory, Probing Single Molecules and Single Nanoparticles by Surface-Enhanced Raman Scattering, Science (80-.). 275 (1997) 1102–1106.

[17] A.J. Haes, C.L. Haynes, A.D. Mcfarland, G.C. Schatz, R.P. Van Duyne, S. Zou, Plasmonic Materials for Surface-Enhanced Sensing and Spectroscopy, MRS Bull. 30 (2005) 368–375.

[18] G.L. Liu, Y. Long, Y. Choi, T. Kang, L.P. Lee, Quantized plasmon quenching dips nanospectroscopy via plasmon resonance energy transfer, Nat. Methods. 4 (2007) 1015–1017.

[19] Y. Choi, T. Kang, L.P. Lee, Plasmon resonance energy transfer (PRET)-based molecular Imaging of cytochrome c in living cells, Nano Lett. 9 (2009) 85–90.

[20] H. Atwater, A. Polman, Plasmonics for improved photovoltaic devices, Nat. Mater. 9 (2010) 205–13.

[21] L. Novotny, S.J. Stranick, Near-filed optical microscopy and spectroscopy with pointed probes, Annu. Rev. Phys. Chem. 57 (2006) 303–331.

[22] F. Vollmer, S. Arnold, Whispering-gallery-mode biosensing : label- free detection down to single molecules, Nat. Methods. 5 (2008) 591–596.

[23] P. Alivisatos, The use of nanocrystals in biological detection, Nat. Biotechnol. 22 (2004) 47–52.

[24] N.R. Guydosh, S.M. Block, Direct observation of the binding state of the kinesin head to the microtubule., Nature. 461 (2009) 125–8.

[25] S.E. Lee, G.L. Liu, F. Kim, L.P. Lee, Remote optical switch for localized and selective control of gene interference, Nano Lett. 9 (2009) 562–570.

[26] J.R. Lakowicz, Principles of fluorescence spectroscopy, 3rd ed., Springer, 2006.

[27] M. Svedendahl, S. Chen, A. Dmitriev, M. Käll, Refractometric sensing using propagating versus localized surface plasmons: a direct comparison., Nano Lett. 9 (2009) 4428–33.

[28] E.C. Le Ru, P.G. Etchegoin, P.D. Diderot, C. Umr, D. Brosse, Mechanisms of spectral profile modification in surface-enhanced fluorescence, J. Phys. Chem. C. 111 (2007) 16076–16079.

[29] B. Sharma, R.R. Frontiera, A. Henry, E. Ringe, R.P. Van Duyne, SERS : Materials , applications , and the future Surface enhanced Raman spectroscopy (SERS) is a powerful vibrational, 15 (2012) 16–25.

[30] N.T. Fofang, T.-H. Park, O. Neumann, N.A. Mirin, P. Nordlander, N.J. Halas, Plexcitonic nanoparticles: plasmon-exciton coupling in nanoshell-J-aggregate complexes., Nano Lett. 8 (2008) 3481–7.

[31] K.M. Birnbaum, A. Boca, R. Miller, A.D. Boozer, T.E. Northup, H.J. Kimble, Photon blockade in an optical cavity with one trapped atom, Nature. 436 (2005) 87–90.

[32] A. Manjavacas, P. Nordlander, F.G. de Abajo, Plasmon blockade in nanostructured graphene, ACS Nano. 6 (2012) 1724–1731.

[33] F.Y. Hong, S.J. Xiong, Single-photon transistors based on the interaction of an emitter and surface plasmons, Nanoscale Res. Lett. 3 (2008) 361–364.

[34] P. Kolchin, R.F. Oulton, X. Zhang, Nonlinear quantum optics in a waveguide: distinct single photons strongly interacting at the single atom level, Phys. Rev. Lett. 106 (2011) 113601.

[35] J.A. Hutchison, T. Schwartz, C. Genet, E. Devaux, T.W. Ebbesen, Modifying chemical landscapes by coupling to vacuum fields., Angew. Chem. Int. Ed. Engl. 51 (2012) 1592–6.

[36] T. Coenen, F. Bernal Arango, a Femius Koenderink, A. Polman, Directional emission from a single plasmonic scatterer., Nat. Commun. 5 (2014) 3250.

[37] K.M. Mayer, J.H. Hafner, Localized surface plasmon resonance sensors, Chem. Rev. 111 (2011) 3828–57.

[38] H. Chen, G.C. Schatz, M.A. Ratner, Experimental and theoretical studies of plasmon-molecule interactions., Rep. Prog. Phys. 75 (2012) 096402.

[39] S.A. Maier, Plasmonics: fundamentals and applications, 2007 editi, Springer, 2007.

[40] C.F. Bohren, D.R. Huffman, Absorption and scattering of light by small particles, Wiley-VCH, 1998.

[41] B. Saleh, M. Teich, Fundamental of photonics, Second edi, John Wiley & Sons, Inc., Hoboken, New Jersey, 2007.

[42] K. Srinivasan, M. Borselli, O. Painter, A. Stintz, S. Krishna, Cavity Q, mode volume, and lasing threshold in small diameter AlGaAs microdisks with embedded quantum dots., Opt. Express. 14 (2006) 1094–105.

[43] M. Barth, S. Schietinger, S. Fischer, J. Becker, N. Nüsse, T. Aichele, et al., Nanoassembled plasmonic-photonic hybrid cavity for tailored light-matter coupling., Nano Lett. 10 (2010) 891–5.

[44] R. Ameling, H. Giessen, Cavity plasmonics: large normal mode splitting of electric and magnetic particle plasmons induced by a photonic microcavity, Nano Lett. 10 (2010) 4394–8.

[45] S.-C. Cheng, T.-C. Wen, Y.-C. Lan, Plasmonic cavities derived from silver nanoparticles atop a massed silver surface for surface enhancement Raman scattering, RSC Adv. 4 (2014) 44457–44461.

[46] S. Kawata, Y. Inouye, P. Verma, Plasmonics for near-field nano-imaging and superlensing, Nat. Photonics. 3 (2009) 388–394.

[47] P. Mühlschlegel, H.-J. Eisler, O.J.F. Martin, B. Hecht, D.W. Pohl, Resonant optical antennas., Science. 308 (2005) 1607–9.

[48] L.O. Herrmann, V.K. Valev, C. Tserkezis, J.S. Barnard, S. Kasera, O.A. Scherman, et al., Threading plasmonic nanoparticle strings with light, Nat. Commun. 5 (2014) 4568.

[49] P.J. Schuck, D.P. Fromm, A. Sundaramurthy, G.S. Kino, W.E. Moerner, Improving the mismatch between light and nanoscale objects with gold bowtie nanoantennas, Phys. Rev. Lett. 94 (2005) 017402.

[50] F. Wang, Y. Shen, General properties of local plasmons in metal nanostructures, Phys. Rev. Lett. 97 (2006) 206806.

[51] R. Marty, G. Baffou, a Arbouet, C. Girard, R. Quidant, Charge distribution induced inside complex plasmonic nanoparticles., Opt. Express. 18 (2010) 3035–44.

[52] F.P. Schmidt, H. Ditlbacher, F. Hofer, J.R. Krenn, U. Hohenester, Morphing a plasmonic nanodisk into a nanotriangle., Nano Lett. 14 (2014) 4810–5.

[53]   C. Sönnichsen, T. Franzl, T. Wilk, G. von Plessen, J. Feldmann, Drastic reduction of plasmon damping in gold nanorods, Phys. Rev. Lett. 88 (2002) 077402.

[54]   A. Wokaun, J. Gordon, P. Liao, Radiation damping in surface-enhanced raman scattering, Phys. Rev. Lett. 48 (1982) 957–960.

[55]   J.D. Jackson, Classical electrodynamics, John Wiley & Sons, Inc., New York, 1975.

[56]   M. Kuttge, E.J.R. Vesseur, J. Verhoeven, H.J. Lezec, H.A. Atwater, A. Polman, Loss mechanisms of surface plasmon polaritons on gold probed by cathodoluminescence imaging spectroscopy, Appl. Phys. Lett. 93 (2008) 113110.

[57]   P. Dawson, K.B. Alexander, J.R. Thompson, J.W. Haas III, T.L. Ferrell, Influence of metal grain size on surface-enhanced Raman scattering, Phys. Rev. B. 44 (1991) 6372–6381.

[58]   J. Krenn, A. Dereux, J. Weeber, E. Bourillot, Y. Lacroute, J. Goudonnet, et al., Squeezing the optical near-field zone by plasmon coupling of metallic nanoparticles, Phys. Rev. Lett. 82 (1999) 2590–2593.

[59]   F. Verstraete, M.M. Wolf, J. Ignacio Cirac, Quantum computation and quantum-state engineering driven by dissipation, Nat. Phys. 5 (2009) 633–636.

[60]   G. Khitrova, H.M. Gibbs, M. Kira, S.W. Koch, A. Scherer, D. Marburg, Vacuum Rabi splitting in semiconductors, (n.d.).

[61]   R. Zia, Optical antennas: redirecting single molecules, Nat. Photonics. 2 (2008) 213–214.

[62]   D. Dregely, R. Taubert, J. Dorfmüller, R. Vogelgesang, K. Kern, H. Giessen, 3D optical Yagi-Uda nanoantenna array., Nat. Commun. 2 (2011) 267.

[63]   T. Pakizeh, M. Käll, Unidirectional ultracompact optical nanoantennas, Nano Lett. 9 (2009) 2343–2349.

[64]   T.H. Taminiau, F.D. Stefani, F.B. Segerink, N.F. van Hulst, Optical antennas direct single-molecule emission, Nat. Photonics. 2 (2008) 234–237.

[65]   C.A. Balanis, Antenna theory: analysis and design, 3rd Editio, John Wiley & Sons, Inc., 2005.

[66]   R. de Waele, A.F. Koenderink, A. Polman, Tunable nanoscale localization of energy on plasmon particle arrays, Nano Lett. 7 (2007) 2004–2008.

[67] F.J. Rodríguez-Fortuño, G. Marino, P. Ginzburg, D. O'Connor, A. Martínez, G. a Wurtz, et al., Near-field interference for the unidirectional excitation of electromagnetic guided modes., Science. 340 (2013) 328–30.

[68] I.M. Hancu, A.G. Curto, M. Castro-López, M. Kuttge, N.F. van Hulst, Multipolar interference for directed light emission., Nano Lett. 14 (2014) 166–71.

[69] Y. Ji, S. Yang, S. Guo, X. Song, B. Ding, Z. Yang, Bimetallic Ag/Au nanoparticles: A low temperature ripening strategy in aqueous solution, Colloids Surfaces A Physicochem. Eng. Asp. 372 (2010) 204–209.

[70] A.B. Smetana, K.J. Klabunde, C.M. Sorensen, A.A. Ponce, B. Mwale, Low-temperature metallic alloying of copper and silver nanoparticles with gold nanoparticles through digestive ripening., J. Phys. Chem. B. 110 (2006) 2155–8.

[71] P. Berman, E. Arimondo, C. Lin, eds., Advances in atomic, molecular, and optical physics, Elsevier, 2009.

[72] A. Periasamy, R.M. Clegg, FLIM microscopy in biology and medicine, 1 edition, Chapman and Hall/CRC, 2009.

[73] U. Noomnarm, R.M. Clegg, Fluorescence lifetimes: fundamentals and interpretations., Photosynth. Res. 101 (2009) 181–94.

[74] F.M. Zehentbauer, C. Moretto, R. Stephen, T. Thevar, J.R. Gilchrist, D. Pokrajac, et al., Fluorescence spectroscopy of Rhodamine 6G: Concentration and solvent effects., Spectrochim. Acta. A. Mol. Biomol. Spectrosc. 121C (2013) 147–151.

[75] S. Garoff, D. Weitz, T. Gramila, C. Hanson, Optical absorption resonances of dye-coated silver island films, Opt. Lett. 6 (1981) 245–247.

[76] P. Hildebrandt, M. Stockburger, Surface-enhanced resonance Raman spectroscopy of Rhodamine 6G adsorbed on colloidal silver, J. Phys. Chem. 88 (1984) 5935–5944.

[77] K. Kneipp, Y. Wang, H. Kneipp, L. Perelman, I. Itzkan, R. Dasari, et al., Single molecule detection using surface-enhanced Raman scattering (SERS), Phys. Rev. Lett. 78 (1997) 1667–1670.

[78] K. Kneipp, Y. Wang, H. Kneipp, I. Itzkan, R. Dasari, M. Feld, Population pumping of excited vibrational states by spontaneous surface-enhanced Raman scattering, Phys. Rev. Lett. 76 (1996) 2444–2447.

[79] A.M. Michaels, M. Nirmal, L.E. Brus, Surface enhanced Raman spectroscopy of individual Rhodamine 6G molecules on large Ag nanocrystals, J. Am. Chem. Soc. 121 (1999) 9932–9939.

[80] J. Zhao, L. Jensen, J. Sung, S. Zou, G.C. Schatz, R.P. Van Duyne, Interaction of plasmon and molecular resonances for rhodamine 6G adsorbed on silver nanoparticles., J. Am. Chem. Soc. 129 (2007) 7647–56.

[81] Y. Wang, Resonant third-order optical nonlinearity of molecular aggregates with low-dimensional excitons, JOSA B. 8 (1991) 981–985.

[82] M. Van Burgel, D.A. Wiersma, K. Duppen, The dynamics of one-dimensional excitons in liquids, 102 (1995) 20–33.

[83] F. Würthner, T.E. Kaiser, C.R. Saha-Möller, J-aggregates: from serendipitous discovery to supramolecular engineering of functional dye materials, Angew. Chem. Int. Ed. Engl. 50 (2011) 3376–410.

[84] M. Kasha, H. Rawls, M. El-Bayoumi, The exciton model in molecular spectroscopy, Pure Appl. Chem. (1965) 371–392.

[85] M. Pope, C. Swenberg, Electronic processes in organic crystals and polymers, 2nd editio, Oxford University Press, Oxford, 1999.

[86] E.G. McRae, M. Kasha, Enhancement of phosphorescence ability upon aggregation of dye molecules, J. Chem. Phys. 28 (1958) 721.

[87] A. Herz, Aggregation of Sensitizing Dyes in Solution and Their Adsorption Onto Silver Halides, Adv. Colloid Interface Sci. 8 (1977) 237–298.

[88] E. Knapp, Lineshapes of Molecular Aggregates. Exchange Narrowing and Intersite Correlation, Chem. Phys. 85 (1984) 73–82.

[89] A. Eisfeld, J. Briggs, The J-band of organic dyes: lineshape and coherence length, Chem. Phys. 281 (2002) 61–70.

[90] H. Chen, T. Ming, L. Zhao, F. Wang, L.-D. Sun, J. Wang, et al., Plasmon–molecule interactions, Nano Today. 5 (2010) 494–505.

[91] K. Kneipp, H. Kneipp, I. Itzkan, R.R. Dasari, M.S. Feld, Surface-enhanced Raman scattering and biophysics, J. Phys. Condens. Matter. 14 (2002) R597–R624.

[92] G. McNay, D. Eustace, W.E. Smith, K. Faulds, D. Graham, Surface-enhanced Raman scattering (SERS) and surface-enhanced resonance Raman scattering (SERRS): a review of applications., Appl. Spectrosc. 65 (2011) 825–37.

[93] J.R. Lakowicz, Plasmonics in Biology and Plasmon-Controlled Fluorescence, Plasmonics. 1 (2006) 5–33.

[94] M. Agio, D.M. Cano, Nano-optics: The Purcell factor of nanoresonators, Nat. Photonics. 7 (2013) 674–675.

[95] E.M. Purcell, Spontaneous emission probabilities at radio frequencies, Phys. Rev. 69 (1946).

[96] K.H. Drexhage, IV Interaction of Light with Monomolecular Dye Layers, Prog. Opt. 12 (1974) 163–232.

[97] M. Pelton, J. Vukovic, Three-dimensionally confined modes in micropost microcavities: quality factors and Purcell factors, IEEE J. Quantum Electron. 38 (2002) 170–177.

[98]   a F. Koenderink, On the use of Purcell factors for plasmon antennas., Opt. Lett. 35 (2010) 4208–10.

[99] M. Barth, S. Schietinger, S. Fischer, J. Becker, N. Nüsse, T. Aichele, et al., Nanoassembled Plasmonic-Photonic Hybrid Cavity for Tailored Light-Matter Coupling., Nano Lett. (2010) 0–4.

[100] L. Novotny, B. Hecht, Principles of Nano-Optics, 1st Editio, Cambridge University Press, New York, NY, 2006.

[101] J.I. Gersten, A. Nitzan, Accelerated Energy Transfer Between Molecules Near A Solid Particle, Chem. Phys. Lett. 104 (1984) 31–37.

[102] M. Lunz, V.A. Gerard, Y.K. Gun'ko, V. Lesnyak, N. Gaponik, A.S. Susha, et al., Surface plasmon enhanced energy transfer between donor and acceptor CdTe nanocrystal quantum dot monolayers., Nano Lett. 11 (2011) 3341–5.

[103] M. Ouyang, H. Huang, N.C. Shaner, A.G. Remacle, S. a Shiryaev, A.Y. Strongin, et al., Simultaneous visualization of protumorigenic Src and MT1-MMP activities with fluorescence resonance energy transfer, Cancer Res. 70 (2010) 2204–12.

[104] E. Kardash, J. Bandemer, E. Raz, Imaging protein activity in live embryos using fluorescence resonance energy transfer biosensors., Nat. Protoc. 6 (2011) 1835–46.

[105] N.J. Halas, S. Lal, W.-S. Chang, S. Link, P. Nordlander, Plasmons in strongly coupled metallic nanostructures, Chem. Rev. 111 (2011) 3913–61.

[106] L. Novotny, Strong coupling, energy splitting, and level crossings: A classical perspective, Am. J. Phys. 78 (2010) 1199.

[107] H. Chen, L. Shao, K.C. Woo, J. Wang, H.-Q. Lin, Plasmonic–Molecular Resonance Coupling: Plasmonic Splitting versus Energy Transfer, J. Phys. Chem. C. 116 (2012) 14088–14095.

[108] C. Wadell, T. Antosiewicz, C. Langhammer, Optical Absorption Engineering in Stacked Plasmonic Au–SiO2–Pd Nanoantennas, Nano Lett. 12 (2012) 4784–4790.

[109] X. Wu, S.K. Gray, M. Pelton, Quantum-dot-induced transparency in a nanoscale plasmonic resonator, Opt. Express. 18 (2010) 23633–23645.

[110] J. Gersten, A. Nitzan, Spectroscopic properties of molecules interacting with small dielectric particles, J. Chem. Phys. 75 (1981) 1139.

[111] N. Liu, L. Langguth, T. Weiss, J. Kästel, M. Fleischhauer, T. Pfau, et al., Plasmonic analogue of electromagnetically induced transparency at the Drude damping limit., Nat. Mater. 8 (2009) 758–62.

[112] D.F. Walls, G.J. Milbrun, Quantum optics, 2008.

[113] C. Gerry, P. Knight, Introductory Quantum Optics, Cambridge University Press, New York, NY, 2005.

[114] M. Brune, F. Schmidt-Kaler, a. Maali, J. Dreyer, E. Hagley, J. Raimond, et al., Quantum Rabi Oscillation: A Direct Test of Field Quantization in a Cavity, Phys. Rev. Lett. 76 (1996) 1800–1803.

[115] E. Jaynes, F. Cummings, Comparison of Quantum and Semiclassical Radiation Theories with Application to the Beam Maser, Proc. IEEE. 51 (1963) 89–109.

[116] R. Adato, A. Artar, S. Erramilli, H. Altug, Engineered absorption enhancement and induced transparency in coupled molecular and plasmonic resonator systems., Nano Lett. 13 (2013) 2584–91.

[117] M. Fleischhauer, J.P. Marangos, Electromagnetically induced transparency : Optics in coherent media, 77 (2005) 633–673.

[118] N.P. de Leon, B.J. Shields, C.L. Yu, D.E. Englund, A. V. Akimov, M.D. Lukin, et al., Tailoring Light-Matter Interaction with a Nanoscale Plasmon Resonator, Phys. Rev. Lett. 108 (2012) 226803.

[119] Y.-F. Xiao, Y.-C. Liu, B.-B. Li, Y.-L. Chen, Y. Li, Q. Gong, Strongly enhanced light-matter interaction in a hybrid photonic-plasmonic resonator, Phys. Rev. A. 85 (2012) 031805.

[120] T.J. Antosiewicz, S.P. Apell, T. Shegai, Plasmon–Exciton Interactions in a Core–Shell Geometry: From Enhanced Absorption to Strong Coupling, ACS Photonics. 1 (2014) 454–463.

[121] R. Jin, Y. Cao, C. a Mirkin, K.L. Kelly, G.C. Schatz, J.G. Zheng, Photoinduced conversion of silver nanospheres to nanoprisms., Science. 294 (2001) 1901–3.

[122] J.C. Love, L.A. Estroff, J.K. Kriebel, R.G. Nuzzo, G.M. Whitesides, Self-assembled Monolayers of Thiolates on Metals as a Form of Nanotechnology, Chem. Rev. 105 (2005) 1103–69.

[123] P.E. Laibinis, G.M. Whitesides, D.L. Allara, Y.-T. Tao, A.N. Parikh, R.G. Nuzzo, Comparison of the Structures and Wetting Properties of Self-Assembled Monolayers of n-Alkanethiols on the Coinage Metal Surfaces, Cu, Ag, Au, J. Am. Chem. Soc. 113 (1991) 7152–7167.

[124] K. Aslan, V.H. Perez-Luna, Surface Modification of Colloidal Gold by Chemisorption of Alkanethiols in the Presence of a Nonionic Surfactant, Langmuir. 18 (2002) 6059–6065.

[125] N.E. Cant, K. Critchley, H.-L. Zhang, S.D. Evans, Surface functionalisation for the self-assembly of nanoparticle/polymer multilayer films, Thin Solid Films. 426 (2003) 31–39.

[126] J. Zheng, Z. Zhu, H. Chen, Z. Liu, Nanopatterned Assembling of Colloidal Gold Nanoparticles on Silicon, Langmuir. 16 (2000) 4409–4412.

[127] D. Aureau, Y. Varin, K. Roodenko, O. Seitz, O. Pluchery, Y.J. Chabal, Controlled Deposition of Gold Nanoparticles on Well-Defined Organic Monolayer Grafted on Silicon Surfaces, J. Phys. Chem. C. 114 (2010) 14180–14186.

[128] L. Feuz, P. Jönsson, M.P. Jonsson, F. Höök, Improving the limit of detection of nanoscale sensors by directed binding to high-sensitivity areas., ACS Nano. 4 (2010) 2167–77.

[129] M.A. Lieb, J.M. Zavislan, L. Novotny, Single-molecule orientations determined by direct emission pattern imaging, J. Opt. Soc. Am. B. 21 (2004) 1210.

[130] G.A. Kopp, Tunable birefringent filters using liquid crystal variable retarders, in: Proc. SPIE 2265, Polariz. Anal. Meas. II, 193, 1994: pp. 193–201.